Journal of Computational Physics 310 (2016) 381–417

Contents lists available at ScienceDirect

Journal of Computational Physics

www.elsevier.com/locate/jcp

A flexible genuinely nonlinear approach for nonlinear wave propagation, breaking and run-up

A.G. Filippini, M. Kazolea, M. Ricchiuto *

Inria Bordeaux Sud-Ouest, Team CARDAMOM, 200 av. de la vieille tour, 33405 Talence cedex, France

ARTICLE INFO

Article history:
Received 24 June 2015
Received in revised form 20 January 2016
Accepted 21 January 2016
Available online 26 January 2016

Keywords:
Green–Naghdi equations
Hybrid scheme
Finite volumes
Finite elements
Wave breaking
Dispersion error

ABSTRACT

In this paper we evaluate hybrid strategies for the solution of the Green–Naghdi system of equations for the simulation of fully nonlinear and weakly dispersive free surface waves. We consider a two step solution procedure composed of: a first step where the non-hydrostatic source term is recovered by inverting the elliptic coercive operator associated to the dispersive effects; a second step which involves the solution of the hyperbolic shallow water system with the source term, computed in the previous phase, which accounts for the non-hydrostatic effects. Appropriate numerical methods, that can be also generalized on arbitrary unstructured meshes, are used to discretize the two stages: the standard C^0 Galerkin finite element method for the elliptic phase; either third order Finite Volume or third order stabilized Finite Element method for the hyperbolic phase. The discrete dispersion properties of the fully coupled schemes obtained are studied, showing accuracy close to or better than that of a fourth order finite difference method. The hybrid approach of locally reverting to the nonlinear shallow water equations is used to recover energy dissipation in breaking regions. To this scope we evaluate two strategies: simply neglecting the non-hydrostatic contribution in the hyperbolic phase; imposing a tighter coupling of the two phases, with a wave breaking indicator embedded in the elliptic phase to smoothly turn off the dispersive effects. The discrete models obtained are thoroughly tested on benchmarks involving wave dispersion, breaking and run-up, showing a very promising potential for the simulation of complex near shore wave physics in terms of accuracy and robustness.

1. Introduction

The accurate mathematical and numerical simulations of water wave propagation in near-shore regions have received considerable attention in the last decades, since they have largely replaced laboratory experiments in the coastal engineering community. Significant efforts have been made in the development of depth averaged models or in the improvement of the existing ones, in order to give accurate description of the nonlinear and non-hydrostatic propagation over complex bathymetries.

The use of asymptotic depth averaged models on this task is quite common, since they lead to numerical models that are of practical use in design compared to the ones produced by more complicated mathematical models like the Euler equations. One of the most known depth averaged models, widely used, is the non-linear shallow water equations (NLSW). This set of equations is capable of providing a good description of the non-linear transformation of the waves, including also

* Corresponding author.
E-mail addresses: andrea.filippini@inria.fr (A.G. Filippini), maria.kazolea@inria.fr (M. Kazolea), mario.ricchiuto@inria.fr (M. Ricchiuto).

http://dx.doi.org/10.1016/j.jcp.2016.01.027
0021-9991/

wave breaking but they lack on describing all the dispersive effects that play an important role on deeper waters and on wave shoaling. As to take into account the dispersion effects, the use of asymptotic depth averaged Boussinesq and enhanced Boussinesq [54,48,46,10,80] type models is quite common. A review on the history and all the fundamental aspects of the Boussinesq-type models can be found in [15].

In the last decades a system of equations, produced by the Euler equations, has gained a lot of attention. Green and Naghdi [31] derived a fully non-linear and weakly dispersive set of equations for an uneven bottom, which represents a two dimensional extension of the Serre equations [66]. They are known as Serre or Green–Naghdi (GN), or fully non-linear Boussinesq equations. The range of validity of the model may vary as much as far the non-linearity parameter ϵ (defined as the ratio of wave amplitude to water depth A/h_0) is concerned, but it requires the shallowness parameter μ (defined as the water depth to wavelength ratio h_0/L) to be small (less than one). The GN model has been fully justified mathematically [40] in the sense that the error between the solutions of the GN system and the Euler equations is small and of size $O(\mu^2)$. We refer to [41,12] for more details.

From the numerical point of view the GN equations have been discretized using different numerical techniques like Finite Differences (FD), Finite Elements (FE) and Finite Volume (FV) approaches. We refer to [3,22,23,20,12,42,44,50,27] among others. For example, in [22,23] the authors derive a higher order FV scheme in one dimension. In [20,12] a hybrid FV/FD splitting approach is used, while [42] follows the same idea for the solution of a new class of two-dimensional GN equations on structured meshes. In [44] a coupled Discontinuous Galerkin and Continuous Galerkin method is developed in one dimension but using only flat bottom topographies. Most of them are also really hard to extend in two dimensions. Up to now and to the authors knowledge there is no work that involves the solution of the later equations in 2D unstructured meshes.

Like all the Boussinesq-type models, GN equations cannot reproduce the energy dissipation that take place when a wave is breaking, producing satisfactory results only outside the breaking region. For this reason the numerical model must be incorporated with a wave breaking mechanism as to handle broken waves. Several approaches have been developed among the years. An extensive review of the existing wave breaking techniques can be found in [37].

In this work, our first aim is to evaluate a strategy that can be easily generalized on arbitrary unstructured meshes, and in the multidimensional case, for the solution of fully nonlinear, weakly dispersive free surface waves. For this reason we consider the hybrid approach, used e.g. in [12] and [37], simulating the propagation and shoaling by means of the Green–Naghdi partial differential equations (PDEs), while locally reverting to the non-linear shallow water equations to model energy dissipation in breaking regions. Starting from the form of the Green–Naghdi equations proposed in [12] and [20], we consider a two step solution procedure: an elliptic phase in which a source term is computed by inverting the coercive operator associated to the dispersive effects; an hyperbolic phase in which the flow variables are evolved by solving the nonlinear shallow water equations, with all the non-hydrostatic effects accounted for by the source computed in the elliptic phase. For the numerical discretization of these two steps we consider methods which can be easily generalized on arbitrary unstructured meshes in the multidimensional case. In particular, we focus on the use of a standard C^0 Galerkin finite element method for the elliptic phase, while high order finite volume (FV) and stabilized finite element (FE) methods are used independently in the hyperbolic phase. The discrete dispersion properties of the fully coupled methods obtained are also studied, showing phase accuracy very close to that of a fourth order finite difference method.

In addition, we will exploit the two step solution procedure to obtain a robust embedding of wave breaking. We evaluate two strategies: one, based on simply neglecting the non-hydrostatic contribution in the hyperbolic phase; the second, involving a tighter coupling of the two phases, with a wave breaking indicator embedded in the elliptic phase to smoothly turn off the dispersive effects. The discrete models obtained are thoroughly tested on benchmarks involving wave dispersion, breaking and run-up, showing a very promising potential for the simulation of complex near shore wave physics.

The paper is organized as follows: The second section describes the mathematical model and the notation used in this work. Then, the equations are re-written obtaining an elliptic–hyperbolic decoupling and the details of two discretization strategies are presented. Section four completes the description of the basic discretizations with a discussion on the time integration schemes along with boundary condition treatment and friction. In section five, the dispersion behavior of both the spatial and temporal discretizations is analyzed in detail, while two alternative ways of embedding wave breaking are proposed in section six. Finally, in section seven, the performance of the proposed methodology is extensively validated against experimental measurements from a series of relevant benchmark problems.

2. The physical model

In this work we refer to the improved Green–Naghdi (GN) system of equations in the form proposed in [12]. This formulation has been recovered by adding some terms of $O(\mu^2)$ to the momentum equation in order to improve the frequency dispersion description of the original GN model. In the following we use the notation sketched in Fig. 1, thus we denote by $h(x,t) = h_0 + \eta(x,t) - b(x)$ the total water depth and by $u(x,t)$ the flow velocity (being $\eta(x,t)$ the free surface elevation with respect to the water rest state, h_0 a reference depth and $b(x)$ the topography variation).

The system of equations can be written in its one-dimensional form as:

$$h_t + (hu)_x = 0 \tag{1}$$

$$(I + \alpha\mathcal{T})\left[(hu)_t + (hu^2)_x + g\frac{\alpha - 1}{\alpha}h\eta_x\right] + \frac{g}{\alpha}h\eta_x + h\mathcal{Q}(u) = 0$$

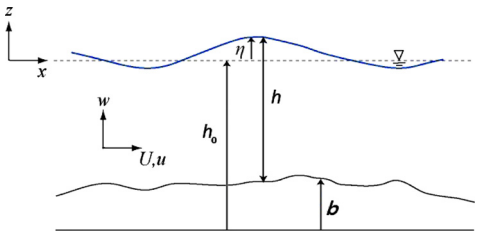

Fig. 1. Sketch of the free surface flow problem, main parameter description.

where the non-linear operator $\mathcal{Q}(\cdot)$ is defined by

$$\mathcal{Q}(\cdot) = 2hh_x(\cdot)_x^2 + \frac{4}{3}h^2(\cdot)_x(\cdot)_{xx} + b_x h(\cdot)_x^2 + b_{xx}h(\cdot)(\cdot)_x + \left[b_{xx}h_x + \frac{1}{2}hb_{xxx} + b_x b_{xx}\right](\cdot)^2 \tag{2}$$

The operator $\mathcal{T}(\cdot)$ plays a key role, as its inversion is necessary to be able to obtain evolution equations for the physical variables. For this reason, following [2] it is important to stress that $\mathcal{T}(\cdot)$ can be written in a compact form involving two operators $S_1(\cdot)$ and $S_2(\cdot)$ and their adjoints $S_1^*(\cdot)$ and $S_2^*(\cdot)$, namely

$$\mathcal{T}(\cdot) = S_1^*\left(hS_1\left(\frac{(\cdot)}{h}\right)\right) + S_2^*\left(hS_2\left(\frac{(\cdot)}{h}\right)\right) \tag{3}$$

where, in multiple space dimensions

$$S_1(\cdot) = \frac{h}{\sqrt{3}}\nabla\cdot(\cdot) - \frac{\sqrt{3}}{2}\nabla b\cdot(\cdot), \qquad S_2(\cdot) = \frac{1}{2}\nabla b\cdot(\cdot) \tag{4}$$

reducing in 1D to

$$S_1(\cdot) = \frac{h}{\sqrt{3}}(\cdot)_x - \frac{\sqrt{3}}{2}b_x(\cdot), \qquad S_2(\cdot) = \frac{1}{2}b_x(\cdot) \tag{5}$$

Note that this formulation is essential to show the coercivity of the operator $I+\alpha\mathcal{T}$, via the corresponding variational form of $\mathcal{T}$:

$$a_{\mathcal{T}}(v,\phi) = \int_\Omega S_1(v)\,h\,S_1\left(\frac{\phi}{h}\right) + \int_\Omega S_2(v)\,h\,S_2\left(\frac{\phi}{h}\right) \tag{6}$$

The interested reader can refer to [2] for details concerning the coercivity analysis. In the above expressions, α is a parameter which is used to improve the dispersion properties of the model in order to obtain a good match with respect to the linearized full Euler equations. The linear dispersion relation of this model can be recovered in the very classical way [47], by introducing in the linearized version of system (1) a solution $W=[h,hu]^T$ expressed in the form of a Fourier mode $W = W_0\exp^{\nu t+jkx}$, with $\nu=\xi+j\omega$ (ω denoting the phase of the mode, ξ representing the rate of amplification/damping and k representing the wavenumber of the Fourier mode). The following dispersion relation can be found in this way:

$$\omega^2 = gh_0k^2\frac{1+\frac{\alpha-1}{3}k^2h_0^2}{1+\frac{\alpha}{3}k^2h_0^2}. \tag{7}$$

Following [42], the value of the parameter α which optimizes the above relation is $\alpha=1.159$, while the system (1) recovers the classical GN equations when $\alpha=1$. According to [42] the above formulation does not require the computation of third order derivatives, while this is necessary in the standard formulation of the GN system. Moreover, the presence of the operator $(I+\alpha\mathcal{T})$ makes the model very stable with respect to high frequency perturbations, which is of highest interest for numerical computations.

3. Discretization strategy: elliptic–hyperbolic decoupling

To discretize system (1) we first recast it in the following way:

$$\begin{aligned} h_t + (hu)_x &= 0 \\ (I+\alpha\mathcal{T})\left[(hu)_t + (hu^2)_x + gh\eta_x\right] - \mathcal{T}(gh\eta_x) + h\mathcal{Q}(u) &= 0 \end{aligned} \tag{8}$$

This allows the operator $(I+\alpha\mathcal{T})$ to be applied to the full shallow water residual. This form suggests a possible decoupling of the elliptic part of the problem from the hyperbolic one, which is obtained as follows:

$$(I + \alpha\mathcal{T})\,\phi = \mathcal{W} - \mathcal{R} \tag{9}$$

$$h_t + (hu)_x = 0 \tag{10}$$

$$(hu)_t + (hu^2)_x + gh\eta_x = \phi$$

having also defined $\mathcal{W} = g\mathcal{T}(h\eta_x)$ and $\mathcal{R} = h\mathcal{Q}(u)$. Given an initial solution, the system above can now be solved in two independent steps:

1. An elliptic step solving for the non-hydrostatic term ϕ;
2. An hyperbolic step evolving the flow variables.

Note that our formulation differs from the ones previously proposed in literature (see e.g. [27]) as it allows the enhancement of an existing shallow water code by the addition of a purely algebraic term to the discrete momentum balance. It has the additional advantage of being a priori able to embed wave breaking effects in the elliptic phase, thus remaining completely non-intrusive w.r.t. the hyperbolic code. To evaluate this simplified and flexible strategy, we will investigate the accuracy and robustness obtainable when the two steps above are each solved with a different numerical method. Our aim is to allow the choice of the method most appropriate and efficient for each step and to provide a simple technique to enhance shallow water codes including genuinely nonlinear dispersive effects.

Note also that we purposely use here the word decoupling and not splitting. Indeed, *the elliptic phase does not involve any time derivative*, so this is not a splitting method, at least not in the sense used in [12] or in [69]. In particular, our approach provides an unsplit spatial discretization of

$$h_t + (hu)_x = 0$$

$$(hu)_t + (hu^2)_x + gh\eta_x = (I + \alpha\mathcal{T})^{-1}\left[\mathcal{T}(gh\eta_x) - h\mathcal{Q}(u)\right]$$

This results in systems of Ordinary Differential Equations (ODEs), which can be evolved in time by any of the known high order time integration methods *without any other source of error that the truncation of the spatial discretizations involved and of the ODE integrators.*

Based on the authors' previous work, we have chosen to implement a standard C^0 Galerkin finite element method for the elliptic phase and to discretize the hyperbolic part by either a high order finite volume (FV), or by a stabilized continuous finite element (FE) method. Time integration is performed with three different methods, involving both multi-stage and multi-step approaches. The resulting hybrid algorithms are analyzed and compared. Of course, other hybrid methods can be obtained e.g. by choosing different approaches for the hyperbolic phase, as e.g. the discontinuous Galerkin method [83,82], the residual distribution method [58], or other time discretization techniques. These different formulations will be discussed in future works.

Here we will study the potential of a formulation which can be easily generalized on arbitrary unstructured meshes. In particular, we will consider the method obtained by only inverting in the elliptic phase the matrices generated when considering a P^1 finite element approximation. As we will show, provided that a third order method is used in the hyperbolic phase, this choice already gives dispersion properties equivalent to those of a fourth order method. As we will see later, the additional advantage of this approach is to allow a direct embedding of wave breaking either by simply neglecting the non-hydrostatic contribution in the hyperbolic phase, or even with a tighter coupling of the two phases using the breaking indicator to smoothly turn off ϕ in the elliptic phase.

The objective of the following sections is to discuss the methods used in this paper. The analysis of the dispersion error of the resulting scheme is then provided in section 5, while the treatment of wave breaking is discussed in section 6.

3.1. Spatial domain discretization and notation

Let $[0, L]$ be the spatial domain, we consider a tessellation composed of elements $[x_i, x_{i+1}]$. We set in general $\Delta x = \min_i(x_{i+1} - x_i)$. For simplicity we assume in the following that the points are equally spaced, so that $x_{i+1} - x_i = \Delta x \ \ \forall i$, but non-uniform meshes can be used with the same methods discussed here with very little modifications. For a given node i, we will denote by C_i the cell $[x_{i-1/2}\, x_{i+1/2}]$, with $x_{i+1/2} - x_{i-1/2} = \Delta x$.

On this mesh, we will denote by φ_i the standard hat shaped C^0 continuous Lagrange basis functions, and we will denote by $\mathbf{U}_{\Delta x}$ the piecewise continuous polynomial obtained as

$$\mathbf{U}_{\Delta x}(x, t) = \sum_i \varphi_i(x)\mathbf{U}_i(t)\,.$$

In this paper we consider the case of P^1 piecewise linear polynomials.

3.2. Elliptic phase: continuous finite element formulation

The first step for solving system (10) is to compute separately the value of the auxiliary variable ϕ from (9). In this work we discretize equation (9) by means of a standard C^0 Galerkin finite element approach. This discretization strategy passes

by the writing of the variational form of the equation. The actual discretization is obtained by evaluating all the integrals by a numerical quadrature over each element of the discretization, with the assumption of piecewise linear variation of all the quantities involved $h_{\Delta x}$, $\eta_{\Delta x}$, $b_{\Delta x}$, $u_{\Delta x}$, $\phi_{\Delta x}$. Defining $\Phi = [\phi_1(t), \phi_2(t), \ldots, \phi_N(t)]^T$ and $U = [u_1(t), u_2(t), \ldots, u_N(t)]^T$, the final form of the Galerkin approximation of the problem can be written as:

$$(\mathrm{M}^{\mathrm{G}} + \alpha \mathrm{T})\Phi = \mathrm{W} - \mathrm{R} \tag{11}$$

$$\mathrm{W} = \mathrm{T}\delta \tag{12}$$

$$\mathrm{R} = \mathrm{Q}[h, U] \tag{13}$$

with δ an approximation of $gh\,\eta_x$. The matrix M^{G} is the Galerkin mass matrix, whose entries are

$$\mathrm{M}^{\mathrm{G}}_{i,j} = \int_0^L \varphi_i \varphi_j \tag{14}$$

The matrix $\mathrm{T}(h_{\Delta x}, b_{\Delta x})$ is deduced immediately from the variational form (6), by evaluating $a_{\mathcal{T}}(\varphi_i, \varphi_j)$. All computations done, we obtain (partial derivatives now denoted by $\partial_{(\cdot)}$ for the sake of clarity)

$$\begin{aligned}\mathrm{T}_{i,j}(h_{\Delta x}, b_{\Delta x}) = {} & \frac{1}{3}\int_0^L \partial_x\varphi_i\, h_{\Delta x}^2\, \partial_x\varphi_j \;-\; \frac{1}{3}\int_0^L \partial_x\varphi_i\, h_{\Delta x}\, \partial_x h_{\Delta x}\, \varphi_j \;+ \\ & + \frac{1}{2}\int_0^L \varphi_i\, \partial_x b_{\Delta x}\, \partial_x h_{\Delta x}\, \varphi_j \;-\; \frac{1}{2}\int_0^L \partial_x\varphi_i\, h_{\Delta x}\, \partial_x b_{\Delta x}\, \varphi_j \;+ \\ & - \frac{1}{2}\int_0^L \varphi_i\, h_{\Delta x}\, \partial_x b_{\Delta x}\, \partial_x\varphi_j \;+\; \int_0^L \varphi_i\, (\partial_x b_{\Delta x})^2\, \varphi_j\end{aligned} \tag{15}$$

having developed all the derivatives of $1/h_{\Delta x}$ terms in order to explicitly remove the singularity w.r.t. h.

Proceeding similarly, we obtain for the operator $\mathrm{Q}(h_{\Delta x}, u_{\Delta x}, b_{\Delta x}, \delta_{b\Delta x})$

$$\begin{aligned}\mathrm{Q}_{i,j}(h_{\Delta x}, u_{\Delta x}, b_{\Delta x}, \delta_{b\Delta x}) = {} & -\frac{2}{3}\int_0^L \partial_x\varphi_i\, h_{\Delta x}^3\, (\partial_x u_{\Delta x})^2 \;+\; \int_0^L \varphi_i\, \partial_x b_{\Delta x}\, h_{\Delta x}^2\, (\partial_x u_{\Delta x})^2 \;+ \\ & + \int_0^L \varphi_i\, \delta_{b\Delta x}\, h_{\Delta x}^2\, u_{\Delta x}\, \partial_x u_{\Delta x} \;+\; \int_0^L \varphi_i\, \delta_{b\Delta x}\, h_{\Delta x}\, \partial_x h_{\Delta x}\, u_{\Delta x} \;+ \\ & + \frac{1}{2}\int_0^L \varphi_i\, \partial_x\delta_{b\Delta x}\, h_{\Delta x}^2\, u_{\Delta x} \;+\; \int_0^L \varphi_i\, \partial_x b_{\Delta x}\, \delta_{b\Delta x}\, h_{\Delta x}\, u_{\Delta x}\end{aligned} \tag{16}$$

The arrays δ and δ_b contain nodal values of auxiliary variables introduced to handle the third order derivatives. In particular, we have

$$(\mathrm{M}^{\mathrm{G}}\delta)_i = \int_0^L \varphi_i\, g\, h_{\Delta x}\, \partial_x\eta_{\Delta x} \tag{17}$$

$$(\mathrm{M}^{\mathrm{G}}\delta_b)_i = -\int_0^L \partial_x\varphi_i\, \partial_x b_{\Delta x} \tag{18}$$

The linear systems (17) and (18) can be solved very efficiently, being M^{G} symmetric, positive defined and constant. On the contrary, the properties of the matrix $(\mathrm{M}^{\mathrm{G}} + \alpha\mathrm{T})$ cannot be known *a priori*. However, the continuous finite element formulation used here inherits the coercivity property of the corresponding continuous operator $\mathcal{T}$, for which the interested reader can refer to [2]. While ensuring the existence of an inverse for this matrix, its computation, required in the solution of the linear algebraic system (11), remains the most computationally demanding process of our approach. In particular, matrix inversions have been performed using the `SPARSEKIT` package [64]. For the M^{G} matrix, we have stored the constant LU decomposition, which, on the contrary, has to be re-computed at each time step for $(\mathrm{M}^{\mathrm{G}} + \alpha\mathrm{T})$.

The kind of discretization performed allows many degrees of freedom in the management of the several Galerkin mass matrices M^{G} which appear in it and that can be lumped (or not) always remaining second order accurate. The optimization of the linear dispersion properties of the resulting schemes (see section 5), together with the research of the simplest configuration possible, led us to the choice of performing the lumping only in equation (18). This does not affect the linear dispersion properties of the scheme, due to the fact that Q is nonlinear and that b is time-independent; so δ_b can be computed once at the beginning of the calculus and kept all along the simulation.

3.3. Hyperbolic phase: Finite Volume scheme

Setting $\mathbf{U} = [h,\, hu]^T$, we will use the FV scheme to write the equations for averages of $\mathbf{U}$ over the cells C_i, namely for

$$\mathbf{U}_i(t) = \frac{1}{\Delta x}\int_{C_i} \mathbf{U}(x,t)\,.$$

Using (9)–(10), and following [9,17,32,53], the semi-discrete form of the equations can now be written as:

$$\frac{d}{dt}\mathbf{U}_i = -\frac{1}{\Delta x}\left[\mathbf{F}_{i+1/2} - \mathbf{F}_{i-1/2}\right] + \frac{1}{\Delta x}\Delta\mathbf{S}_{b\,i} + \overline{\mathbf{\Phi}} \tag{19}$$

where $\mathbf{F}_{i\pm1/2}$ and $\Delta\mathbf{S}_{bi}$ are the numerical fluxes at each cell interface and the numerical topography source respectively. The last term is where the link with the elliptic phase is made. In particular, it stands:

$$\overline{\mathbf{\Phi}} = \frac{1}{\Delta x}\int_{C_i}\begin{pmatrix}0\\ \phi_{\Delta x}\end{pmatrix} = \frac{1}{8}\begin{pmatrix}0\\ \phi_{i-1}+6\phi_i+\phi_{i+1}\end{pmatrix}$$

having integrated exactly over C_i the piecewise linear polynomial $\phi_{\Delta x}$ obtained from the elliptic phase discussed in the previous subsection. The numerical fluxes $\mathbf{F}_{i\pm1/2}$ at the cell interfaces can be evaluated by means of an exact or approximate Riemann solver. In this work we used the approximate Riemann solver of Roe [61] along with an upwind discretization of the topography source. The source terms are numerical treated as to satisfy the C-property and can be easily incorporated in this solver. The numerical fluxes in (19) are defined as:

$$\mathbf{F}_{i+1/2} = \mathbf{F}_{i+1/2}(\mathbf{U}^L_{i+1/2}, \mathbf{U}^R_{i+1/2}) = \frac{1}{2}\left(\mathbf{F}(\mathbf{U}^R_{i+1/2}) + \mathbf{F}(\mathbf{U}^L_{i+1/2})\right) - \frac{1}{2}|\mathbf{A}|_{i+1/2}\Delta_{i+1/2}\mathbf{U} \tag{20}$$

where $\Delta(\cdot)_{i+1/2} = (\cdot)^R_{i+1/2} - (\cdot)^L_{i+1/2}$. $\mathbf{A}_{i+1/2}$ is the Roe average Jacobian matrix and is equal to $\left[\mathbf{X}|\Lambda|\mathbf{X}^{-1}\right]_{i+1/2}$, where $\mathbf{X}_{i+1/2}$ and $\mathbf{X}^{-1}_{i+1/2}$ are the left and right eigenvector matrices respectively and $\mathbf{\Lambda}$ is the diagonal matrix with the eigenvalues in the diagonal.

The numerical integration with the upwind scheme presented up to now lead to approximations that are only first order accurate, if a constant distribution is assumed in each computational cell C_i. To achieve higher accuracy we evaluate the left and right states using a third order MUSCL extrapolation scheme [78,38]. The reconstruction is performed for the variables $[h,\, u]$ as well as for the topography b. For the $(i+1/2)$ interface the reconstructed values of the total water depth can be written as

$$\begin{aligned} h^L_{i+1/2} &= h_i + \frac{\psi(r_i)}{4}\left[(1-\kappa)\Delta h_{i-1/2} + (1+\kappa)\Delta h_{i+1/2}\right] \\ h^R_{i+1/2} &= h_{i+1} - \frac{\psi(r_{i+1})}{4}\left[(1-\kappa)\Delta h_{i+3/2} + (1+\kappa)\Delta h_{i+1/2}\right] \end{aligned} \tag{21}$$

where ψ is the limiter function with $r_i = \frac{\Delta h_{i-1/2}}{\Delta h_{i+1/2}}$, and where third order of accuracy in smooth regions is obtained for $\kappa = 1/3$. In this work the widely known MIN-MODE and MC limiters are used [43].

In the numerical solution, the correct discrete balance between the numerical fluxes and the numerical topography source is very important. A scheme that respects this balance is known in the literature as a well-balanced scheme. As it has been shown in [9], an upwind discretization approach should also be used for the bed topography term $\mathbf{S}_b$ to avoid non-physical oscillations in the solution by satisfying the C-property in hydrostatic flow conditions (flow at rest). To satisfy the exact C-property, the topography source term must be linearized in the same way and evaluated in the same state (Roe-averaged state) as the flux terms. Of course, if an other Riemann solver is employed (e.g. HLL, HLLC) for the computation of the numerical fluxes, a different technique should be used, see for example [62,73]. In this work, following [9,32], the source term in (19) contains the following two terms

$$\Delta\mathbf{S}_{b,\,i} = \mathbf{S}^-_{b,\,i+1/2}(\mathbf{U}^L_{i+1/2}, \mathbf{U}^R_{i+1/2}) + \mathbf{S}^+_{b,\,i-1/2}(\mathbf{U}^L_{i-1/2}, \mathbf{U}^R_{i-1/2}) \tag{22}$$

where

$$\mathbf{S}^{+}_{b\,i+1/2}(\mathbf{U}^{L}_{i+1/2},\mathbf{U}^{R}_{i+1/2}) = \frac{1}{2}\left[\mathbf{X}(\mathbf{I}+\mathbf{\Lambda}^{-1}|\mathbf{\Lambda}|)\mathbf{X}^{-1}\right]_{i+1/2}\widetilde{\mathbf{S}}_{b\,i+1/2}(\mathbf{U}^{L}_{i+1/2},\mathbf{U}^{R}_{i+1/2})$$
$$\mathbf{S}^{-}_{b\,i+1/2}(\mathbf{U}^{L}_{i+1/2},\mathbf{U}^{R}_{i+1/2}) = \frac{1}{2}\left[\mathbf{X}(\mathbf{I}-\mathbf{\Lambda}^{-1}|\mathbf{\Lambda}|)\mathbf{X}^{-1}\right]_{i+1/2}\widetilde{\mathbf{S}}_{b\,i+1/2}(\mathbf{U}^{L}_{i+1/2},\mathbf{U}^{R}_{i+1/2}) \tag{23}$$

and with

$$\widetilde{\mathbf{S}}_{b\,i+1/2}(\mathbf{U}^{L}_{i+1/2},\mathbf{U}^{R}_{i+1/2}) = \left[\begin{array}{c} 0 \\ -g\dfrac{h^{L}+h^{R}}{2}\left(b^{R}-b^{L}\right)\end{array}\right]_{i+1/2}. \tag{24}$$

For the first order scheme, using the relation above, the discretization of the numerical flux term balances with the one of the topography source terms for hydrostatic conditions. This gives in each mesh cell: $u=0$ and $b^{R}-b^{L}=-\left(h^{R}-h^{L}\right)$. While this holds for the first order scheme, this is not the case when using higher reconstructions as we do here. In this case, following [32,53], we include the additional correction term $\mathbf{S}^{\star}_{b}$ for maintaining the correct balance, i.e.

$$\Delta\mathbf{S}_{b\,i} = \mathbf{S}^{-}_{b\,i+1/2} + \mathbf{S}^{+}_{b\,i-1/2} + \mathbf{S}^{\star}_{b}\left(\mathbf{U}^{L}_{i+1/2},\mathbf{U}^{R}_{i-1/2}\right) \tag{25}$$

with

$$\mathbf{S}^{\star}_{b}\left(\mathbf{U}^{L}_{i+1/2},\mathbf{U}^{R}_{i-1/2}\right) = \left[\begin{array}{c} 0 \\ -g\dfrac{h^{R}_{i-1/2}+h^{L}_{i+1/2}}{2}\left(b^{R}_{i-1/2}-b^{L}_{i+1/2}\right)\end{array}\right].$$

3.4. Hyperbolic phase: finite element scheme

Two FE methods are considered here. The first is a classical C^{0} Galerkin approximation of the two equations (10). For an internal node i, the discrete continuous Galerkin equations are readily obtained by evaluating the integrals (set $q=hu$)

$$\int_{0}^{L}\varphi_{i}\partial_{t}h_{\Delta x} - \int_{0}^{L}\partial_{x}\varphi_{i}q_{\Delta x} = 0$$
$$\int_{0}^{L}\varphi_{i}\partial_{t}q_{\Delta x} - \int_{0}^{L}\partial_{x}\varphi_{i}\left[\frac{q^{2}_{\Delta x}}{h_{\Delta x}}+g\frac{h^{2}_{\Delta x}}{2}\right] - \int_{0}^{L}\varphi_{i}\tilde{S}_{b} = \int_{0}^{L}\varphi_{i}\phi_{\Delta x} \tag{26}$$

with $\tilde{S}_{b}=-gh\partial_{x}b$. With the notation of the previous section, the integrals can be approximated as [60]

$$\mathbf{M}^{\mathrm{G}}\frac{d}{dt}\mathbf{U} = -\frac{1}{2}\left[\mathbf{F}(\mathbf{U}_{i+1})-\mathbf{F}(\mathbf{U}_{i-1})\right] + \frac{1}{2}\tilde{\mathbf{S}}_{b\,i+1/2} + \frac{1}{2}\tilde{\mathbf{S}}_{b\,i-1/2} + \overline{\mathbf{\Phi}}^{\mathrm{G}} \tag{27}$$

where $\mathbf{M}^{\mathrm{G}}$ is the Galerkin mass matrix defined in (14).

By analogy with (19), we use the notation $\overline{\mathbf{\Phi}}$ for the contribution of the non-hydrostatic term, which in this case is given by

$$\overline{\mathbf{\Phi}}^{\mathrm{G}} = \mathbf{M}^{\mathrm{G}}\mathbf{\Phi}\,. \tag{28}$$

As shown in [77,60], scheme (27) is fourth order accurate in space on regular meshes, when the shallow water limit is considered.

To obtain a discretization with some shock capturing capabilities, we consider the upwind stabilized method used in [60,6,7] (see also [33]). In particular, introducing the local residual

$$\mathbf{R}_{\Delta x} = \left(\begin{array}{c} \partial_{t}h_{\Delta x}+\partial_{x}q_{\Delta x} \\ \partial_{t}q_{\Delta x}+\partial_{x}(q^{2}_{\Delta x}/h_{\Delta x}+gh^{2}_{\Delta x}/2)-\tilde{S}_{b}-\phi_{\Delta x}\end{array}\right), \tag{29}$$

obtained by replacing in the continuous equations the discrete approximation of the unknowns, we consider the streamline upwind scheme:

$$\mathbf{M}^{\mathrm{G}}\frac{d}{dt}\mathbf{U} = -\frac{1}{2}\left[\mathbf{F}(\mathbf{U}_{i+1})-\mathbf{F}(\mathbf{U}_{i-1})\right] + \frac{1}{2}\tilde{\mathbf{S}}_{b\,i+1/2} + \frac{1}{2}\tilde{\mathbf{S}}_{b\,i-1/2} + \overline{\mathbf{\Phi}}^{\mathrm{G}} - \sum_{j=0}^{1}\int_{x_{i+j-1}}^{x_{i+j}} A\,\partial_{x}\varphi_{i}\,\boldsymbol{\tau}_{\mathrm{SU}}\,\mathbf{R}_{\Delta x}\,.$$

In the last expression, the matrix $\boldsymbol{\tau}_{\mathrm{SU}}$ is a scaling parameter in practice defined as in [33,60]

$$\boldsymbol{\tau}_{\mathrm{SU}} = \frac{\Delta x}{2}|A|^{-1}.$$

With this definition, using (29) and the notation of section 3.2, one easily shows that the streamline upwind scheme can be written as

$$\mathbf{M}^{\mathrm{SU}}\frac{d}{dt}\mathbf{U} = -\left[\mathbf{F}_{i+1/2}(\mathbf{U}_i,\mathbf{U}_{i+1}) - \mathbf{F}_{i+1/2}(\mathbf{U}_{i-1},\mathbf{U}_i)\right] + \mathbf{S}^{-}_{b\,i+1/2}(\mathbf{U}_i,\mathbf{U}_{i+1}) + \mathbf{S}^{+}_{b\,i-1/2}(\mathbf{U}_{i-1},\mathbf{U}_i)\,\overline{\boldsymbol{\Phi}}^{\mathrm{SU}} \tag{30}$$

where the numerical fluxes and sources have exactly the same expression as in (20) and (23) respectively, and where the entries of the Streamline Upwind mass matrix now couple the h and q ODEs and depend on the sign of the shallow water flux Jacobian matrix A. In particular

$$\left[\mathbf{M}^{\mathrm{SU}}\mathbf{V}\right]_i = \frac{\Delta x}{6}\mathbf{V}_{i-1} + \frac{2\Delta x}{3}\mathbf{V}_i + \frac{\Delta x}{6}\mathbf{V}_{i+1} + \frac{\Delta x}{4}\mathrm{sign}(A_{i-1/2})\left(\mathbf{V}_{i-1}+\mathbf{V}_i\right) - \frac{\Delta x}{4}\mathrm{sign}(A_{i+1/2})\left(\mathbf{V}_{i+1}+\mathbf{V}_i\right) \tag{31}$$

By analogy with (19), we have used the notation $\overline{\boldsymbol{\Phi}}$ for the contribution of the non-hydrostatic terms, which in this case is given by

$$\overline{\boldsymbol{\Phi}}^{\mathrm{SU}} = \mathbf{M}^{\mathrm{SU}}\Phi.$$

As shown in [60,6,7], to which we refer for all additional details, the stabilized FE method (30) is third order accurate in space when the shallow water limit is considered, and it preserves exactly steady state still flat free surface states.

Finally, in order to handle moving bores and dry areas, we introduce as in [6,7] the following nonlinear splitting of the mass matrix (sc stands for shock capturing):

$$\begin{aligned}\left[\mathbf{M}^{\text{SU-sc}}\mathbf{V}\right]_i = {} & \Delta x\mathbf{V}_i + \psi_{i+1/2}\frac{\Delta x}{2}\left[\frac{1}{3}\left(\mathbf{V}_{i+1}-\mathbf{V}_i\right) - \frac{\mathrm{sign}(A_{i+1/2})}{2}\left(\mathbf{V}_{i+1}+\mathbf{V}_i\right)\right] \\ & + \psi_{i-1/2}\frac{\Delta x}{2}\left[\frac{1}{3}\left(\mathbf{V}_{i-1}-\mathbf{V}_i\right) + \frac{\mathrm{sign}(A_{i-1/2})}{2}\left(\mathbf{V}_{i-1}+\mathbf{V}_i\right)\right]\end{aligned} \tag{32}$$

The final form of the scheme reads

$$\mathbf{M}^{\text{SU-sc}}\frac{d}{dt}\mathbf{U} = -\left[\mathbf{F}_{i+1/2}(\mathbf{U}_i,\mathbf{U}_{i+1}) - \mathbf{F}_{i+1/2}(\mathbf{U}_{i-1},\mathbf{U}_i)\right] + \mathbf{S}^{-}_{b\,i+1/2}(\mathbf{U}_i,\mathbf{U}_{i+1}) + \mathbf{S}^{+}_{b\,i-1/2}(\mathbf{U}_{i-1},\mathbf{U}_i)\Delta x\,\overline{\boldsymbol{\Phi}}^{\text{SU-sc}} \tag{33}$$

The quantity $\psi_{i\pm1/2}$ in (32) is a limiter function. For $\psi = 0$ the scheme reduces to the first order version of Roe's scheme, which is basically the first order version of (19). For $\psi = 1$ the third order finite element method (30) is recovered. Any function can be used to detect smooth areas and dry or shocked regions.

Here, we use the smoothness sensor proposed in [6,7] and based on two different approximations of the curvature of the free surface elevation η:

$$\psi_{i+1/2} = \min(\psi_i,\psi_{i+1}), \qquad \psi_i = \min\left(1,\ \alpha\frac{|\int_0^L \varphi_i\partial_x\eta_{\Delta x}|}{|\int_0^L \partial_x\varphi_i\partial_x\eta_{\Delta x} + V_i|}\right)$$

where V_i is obtained as the fourth order finite difference approximation of $\partial_{xx}\eta_i$, and with $\alpha = \frac{1}{9}$ as in [6,7].

3.5. Well-balancing, wet/dry front treatment, mass conservation

In order to identify the dry cells we use the technique described in [59,58]. In particular, we introduce two threshold parameters ϵ_h^{wd} and ϵ_u^{wd}, acting independently on the water height and the velocity respectively. So, if H in a node is less that ϵ_h^{wd}, that node is considered as dry. This parameter is very small, compared to the mesh size (typical values range are between 10^{-9} and 10^{-6}). The second parameter is used to avoid division by zero and is set to

$$\epsilon_u^{wd} = \frac{\Delta x^2}{L^2}$$

with L the length of the spatial domain. If in a node $h \le \epsilon_u^{wd}$, the velocity in that node is set to zero. To avoid loosing mass, and guarantee absolute mass conservation, we follow the treatments proposed in [25,16,45] where the total mass in nodes with $h \le \epsilon_u^{wd}$ is redistributed uniformly to the rest of the domain.

Furthermore, the presence of dry areas should not affect the ability of the schemes to preserve steady states involving flat free surface still water. To ensure this property, we use a standard technique consisting in redefining the bed elevation at the emerging dry cell [17,16] as:

$$\Delta b = \begin{cases} h^L & \text{if } h^L > \epsilon_h^{wd} \text{ and } h^R \leq \epsilon_h^{wd} \text{ and } b^R < (b^R - b^L) \\ (b^L - b^R) & \text{otherwise} \end{cases} \tag{34}$$

when a wet/dry front exists between computational cells with (reconstructed) face values L and R. For both FV and FE schemes this modification is applied in the computation of the source term $\tilde{\mathbf{S}}_b$. A similar treatment holds if R is wet and L dry. Just for the FV scheme and for the flow in motion over adverse slopes, further modifications are made following [19,36]. Finally, and as to properly detect regions in proximity of dry areas, we use an exponential filter proposed in [59,58]. This exponential function is embedded in the limiters and activated whenever the limiter is on.

4. Time integration, boundary conditions, and friction

4.1. High order time integration methods

Similarly to the spatial domain, the temporal domain is discretized by a set of non-overlapping slabs $[t^n, t^{n+1}]$. We will denote by $\Delta t^{n+1} = t^{n+1} - t^n$. For generality, three different time discretizations are compared in this work. One is a method quite classical in the context of Boussinesq type numerical models, while the other two have been chosen as representatives of boundedness or strong stability preserving methods. For all of these methods, the time step is computed by means of the CFL condition

$$\Delta t^{n+1} = \text{CFL} \frac{\Delta x}{\max_i(|u_i^n| + \sqrt{g h_i^n})} \tag{35}$$

For the shallow water equations, the stability condition for the first order methods used here is $\text{CFL}_c = 1$ when using the first order explicit Euler method. Following [30,57], we will speak of effective CFL as the ratio CFL_c/p, with p the number of right hand side evaluations in one time step.

The first time integration scheme we consider is the Adams–Bashforth/Adams–Moulton (AM) predictor–corrector method, well known in the community of Boussinesq modelling [79,62]. For the ODE

$$\mathbf{U}' = \mathcal{L}(\mathbf{U}) \tag{36}$$

this time integration scheme requires two stages:

1. Predictor stage (Adams–Bashforth method)

$$\mathbf{U}^p = \mathbf{U}^n + \frac{\Delta t}{12}\left[23\mathcal{L}(\mathbf{U}^n) - 16\mathcal{L}(\mathbf{U}^{n-1}) + 5\mathcal{L}(\mathbf{U}^{n-2})\right] \tag{37}$$

2. Corrector stage (Adams–Moulton method)

$$\mathbf{U}^{n+1} = \mathbf{U}^n + \frac{\Delta t}{24}\left[9\mathcal{L}(\mathbf{U}^p) + 19\mathcal{L}(\mathbf{U}^n) - 5\mathcal{L}(\mathbf{U}^{n-1}) + \mathcal{L}(\mathbf{U}^{n-2})\right] \tag{38}$$

The Adams predictor corrector has stability properties close to those of the explicit Euler scheme, with respect to which we thus have an affective CFL of 1/2 (2 stages for the same time step magnitude). The method is obtained by a combination of Lagrange polynomial extrapolation, and polynomial interpolation to evaluate the integral of $\mathcal{L}$ in the interval $[t^n, t^{n+1}]$ (see e.g. [49], chapter 9). For the autonomous ODE (36), fourth order of accuracy can be easily shown by standard truncation error analysis. The technique used to derive the method can be generalized to include variable time step sizes, but this is way beyond the scope of this paper. A simple technique to account for variable time step sizes, while keeping constant the coefficients in the scheme, is to re-correct iteratively with the Adams–Moulton step, stopping when the relative magnitude of the correction is below a given threshold (cf. [79,28,62]). In practice, however, the improvement brought by this multi-corrector procedure is very small, and a single correction is already enough to obtain accurate results also for variable step sizes (see [79]).

We also test the three stage third order SSP Runge–Kutta (RK3) scheme reading [30]

$$\begin{aligned} \mathbf{U}^p &= \mathbf{U}^n + \Delta t\, \mathcal{L}(\mathbf{U}^n) \\ \mathbf{U}^{2p} &= \frac{3}{4}\mathbf{U}^n + \frac{1}{4}\mathbf{U}^p + \frac{\Delta t}{4}\mathcal{L}(\mathbf{U}^p) \\ \mathbf{U}^{n+1} &= \frac{1}{3}\mathbf{U}^n + \frac{2}{3}\mathbf{U}^{2p} + \frac{2\Delta t}{3}\mathcal{L}(\mathbf{U}^{2p}) \end{aligned} \tag{39}$$

The RK3 belongs to the family of strong stability preserving multi-stage methods with positive coefficients, inheriting the same stability properties of the explicit Euler scheme. In particular, compared to the latter, the RK3 has a CFL condition of 1, giving an effective CFL of 1/3.

Lastly, we have tested the third order extrapolated backward differencing method (eBDF3) [39] reading

$$\alpha_{n+1}\mathbf{U}^{n+1} + \alpha_n\mathbf{U}^n + \alpha_{n-1}\mathbf{U}^{n-1} + \alpha_{n-2}\mathbf{U}^{n-2} = \beta_n\,\mathcal{L}(\mathbf{U}^n) + \beta_{n-1}\,\mathcal{L}(\mathbf{U}^{n-1}) + \beta_{n-2}\,\mathcal{L}(\mathbf{U}^{n-2}) \tag{40}$$

where the weights take the form

$$\alpha_{n+1} = \frac{1}{\Delta t^{n+1}} + \frac{1}{\Delta t^{n+1}+\Delta t^n} + \frac{1}{\Delta t^{n+1}+\Delta t^n+\Delta t^{n-1}}, \quad \alpha_n = -\frac{(\Delta t^{n+1}+\Delta t^n)(\Delta t^{n+1}+\Delta t^n+\Delta t^{n-1})}{\Delta t^{n+1}\Delta t^n(\Delta t^n+\Delta t^{n-1})}$$
$$\alpha_{n-1} = \frac{\Delta t^{n+1}(\Delta t^{n+1}+\Delta t^n+\Delta t^{n-1})}{(\Delta t^{n+1}+\Delta t^n)\Delta t^n\Delta t^{n-1}},$$
$$\alpha_{n-2} = -\frac{\Delta t^{n+1}(\Delta t^{n+1}+\Delta t^n)}{(\Delta t^{n+1}+\Delta t^n+\Delta t^{n-1})(\Delta t^n+\Delta t^{n-1})\Delta t^{n-1}}$$

and

$$\beta_n = \frac{(\Delta t^{n+1}+\Delta t^n)(\Delta t^{n+1}+\Delta t^n+\Delta t^{n-1})}{\Delta t^n(\Delta t^n+\Delta t^{n-1})}, \quad \beta_{n-1} = -\frac{\Delta t^{n+1}(\Delta t^{n+1}+\Delta t^n+\Delta t^{n-1})}{\Delta t^n\Delta t^{n-1}},$$
$$\beta_{n-2} = \frac{\Delta t^{n+1}(\Delta t^{n+1}+\Delta t^n)}{(\Delta t^n+\Delta t^{n-1})\Delta t^{n-1}}$$

The eBDf3 is part of a family of high order explicit multi-step methods verifying, under a time step restriction, the same boundedness preserving property of the explicit Euler scheme. Compared to the latter, the eBDf3 has a stability condition of CFL = 1/3 [34], which gives the same effective CFL of the RK3 method.

4.2. Boundary conditions and internal source function

To define differential problems, boundary conditions must be introduced. In this work we use two types of boundary conditions, depending on the examined test case: solid (reflective) wall and absorbing boundary conditions. For the FV scheme with third-order MUSCL reconstruction, the reconstructed values on the first and last cell of the computational domain are computed using neighboring ghost cells. More informations can be found in [36]. For the FE schemes, ghost cells are in no need since it is a node centered scheme and the degrees of freedom are located directly on the physical boundary.

Absorbing boundaries are also applied in order to dissipate completely the energy of the incoming waves, trying at the same time to eliminate any non-physical reflection. This kind of boundaries requires the definition of a sponge layer in which the surface elevation and the momentum are damped by multiplying their values by a coefficient $m(x)$ defined as [37]

$$m(x) = \sqrt{1 - \left(\frac{x - d(x)}{L_s}\right)^2}. \tag{41}$$

L_s is the sponge layer width and $d(x)$ is the normal distance between the cell center with coordinates x and the absorbing boundary. Typical values for the sponge layer width are related to the wavelenght of the incoming wave: $L \leq L_s \leq 1.5L$. Thus, longer wavelengths require longer sponge layers.

Wave generation in the model is achieved by using the internal wave generator of Wei et al. [81]. In [81] the wave generator of free surface waves is introduced as a source function added to the mass equation. It is derived using the equations of Nwogu [54], but it can be used for many types of Boussinesq-type equations by changing the dispersion relation used in the generator. In this work, as to be compatible with the equations of GN, we use the dispersion relation (7).

4.3. Friction terms discretization

An explicit treatment of the friction can produce numerical oscillations [16,52,51] when the roughness coefficient is high. For this reason, we use the technique proposed in [16,51]. More precisely, for all schemes, at the end of each time step, we have:

$$(hu)_i^{n+1} = (hu)_i^{\star} - g(hS_f)_i^{n+1}\Delta t^n \tag{42}$$

where all the values signed with $\star$ are the values computed without the friction. Using $(S_f)_i = (uR_f)_i = u_i\dfrac{N_m^2||u_i||}{h_i^{4/3}}$ and substituting in the above equation, we have:

$$(hu)_i^{n+1} = (hu)_i^{\star} - g(huR_f)_i^{n+1}\Delta t^n = (hu)_i^{\star} - g(hu)_i^{n+1}\left[(1-\theta)(R_f)_i^{n+1} + \theta(R_f)_i^n\right]\Delta t^n \tag{43}$$

with N_m being the Manning roughness coefficient. Now, by separating explicit and implicit part and by assuming that $R_f^{n+1} = R_f^\star$, we can write:

$$(hu)_i^{n+1} = \frac{(hu)_i^\star - \theta g (hu)_i^n (R_f)_i^n \Delta t^n}{1 + (1-\theta) g (R_f)_i^\star \Delta t^n} \tag{44}$$

When the implicitness parameter θ is set to zero, the friction source term is computed in a completely implicit manner, while it is computed in a totally explicit point wise manner when $\theta = 1$. In all the computations shown in this work the value $\theta = 0$ has been used. This modification, albeit very robust, makes the scheme locally first order in time when friction is dominating. This is especially the case in wet–dry fronts. Techniques to construct high order variants for the eBFD and Runge–Kutta methods are discussed in [35,21], and will be exploited in the future.

5. Semi-discrete error analyses

5.1. Time continuous analysis

The analytical expression of the linear dispersion relation for the present model has been already given in section 2 and will be here rewritten:

$$\omega_{\mathrm{GN}}^2 = g h_0 k^2 \frac{1 + \frac{\alpha - 1}{3} k^2 h_0^2}{1 + \frac{\alpha}{3} k^2 h_0^2}. \tag{45}$$

As already explained, this relation can be recovered by means of a Fourier analysis on a horizontal bottom performed on the linearized system of equations:

$$(I + \alpha T_{LIN})\phi = T_{LIN}(g h_0 \eta_x) \tag{46}$$

$$\begin{aligned} \eta_t + h_0 u_x &= 0 \\ h_0 u_t + g h_0 \eta_x &= \phi \end{aligned} \tag{47}$$

where h_0 represents the constant water depth and $T_{LIN}(\cdot) = -\frac{1}{3} h_0^2 (\cdot)_{xx}$.

Having a low dispersion error w.r.t. the model is of paramount importance for any numerical scheme that wants to be applied to the study of near-shore wave propagation. In this section we will perform an analysis on the discrete dispersion relations of the several schemes here implemented: continuous finite element (with and without the upwind stabilization) and finite volume; comparing them and finding the best possible configuration of the discretization which minimizes the dispersion error.

We perform our analysis replacing the nodal values of η and u in each discretized scheme by a propagating Fourier mode $W_i = W_0 e^{\nu_{\Delta x} t + j k x_i}$; where $\nu_{\Delta x} = \xi_{\Delta x} + j\omega_{\Delta x}$ and $\xi_{\Delta x}$ and $\omega_{\Delta x}$ represent respectively the amplification rate and the phase speed, while k is the wave number of the Fourier mode. The algebraic expression obtained in such a way can be easily rewritten in terms of the nodal value W_i, using relations of the type $W_{i\pm1} = e^{\pm jk\Delta x}$. The resulting system of equations constitutes a complex eigenvalue problem, whose solution is the dispersion factor $\nu_{\Delta x}$.

The dispersion formulae obtained are hard to interpret, so we choose to present the results in the form of comparison plots, in which the dispersion error curves of the model are compared among them and w.r.t. the ones given by second (FD2) and fourth (FD4) order finite different discretization schemes. For the sake of brevity and clarity, in the following, we will just present the concluding remarks. Please refer to the appendix for more details.

5.1.1. Finite element

When also the hyperbolic part is discretized with the centered Galerkin FE scheme described in (27), the system obtained for the nodal values of a Fourier mode is

$$\left(\tilde{\mathrm{M}}^{\mathrm{G}} - \frac{\alpha h_0^2}{3} \tilde{\mathrm{S}}^{\mathrm{G}}\right)\phi_i = -\frac{g h_0^3}{3} \tilde{\mathrm{T}}^{\mathrm{G}} \left(\tilde{\mathrm{M}}^{\mathrm{G}}\right)^{-1} \eta_i \tag{48}$$

$$\begin{aligned} \tilde{\mathrm{M}}^{\mathrm{G}} \nu_{\Delta x} \eta_i + h_0 \tilde{\mathrm{F}}^{\mathrm{G}} u_i &= 0 \\ \tilde{\mathrm{M}}^{\mathrm{G}} \nu_{\Delta x} u_i + g \tilde{\mathrm{F}}^{\mathrm{G}} \eta_i &= \frac{1}{h_0} \tilde{\mathrm{M}}^{\mathrm{G}} \phi_i \end{aligned} \tag{49}$$

While different expressions are obtained for the second and third equations when other schemes are used in the hyperbolic phase, note that the first one remains the same in all the cases considered in the paper. The discrete phase $\omega_{\Delta x}$ is computed by imposing that the above linear system admits a non-trivial solution, and hence that the associated matrix has zero determinant.

The results obtained from (49) are summarized in Fig. 2 in terms of the relative dispersion error w.r.t. the exact phase (7). The curves are obtained for the two values $kh_0 = 0.5$ and $kh_0 = 2.5$, corresponding to a long and to a short(er) wave (or

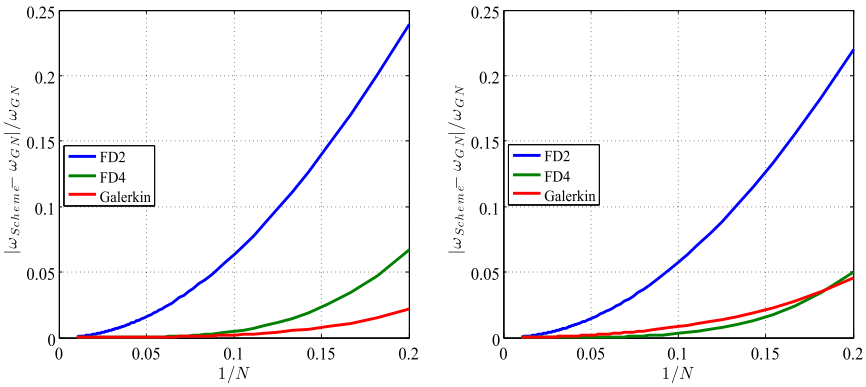

Fig. 2. Dispersion error for the centered Galerkin FE scheme for $kh_0 = 0.5$ (left) and $kh_0 = 2.5$ (right): comparison w.r.t. the FD2 and FD4 schemes.

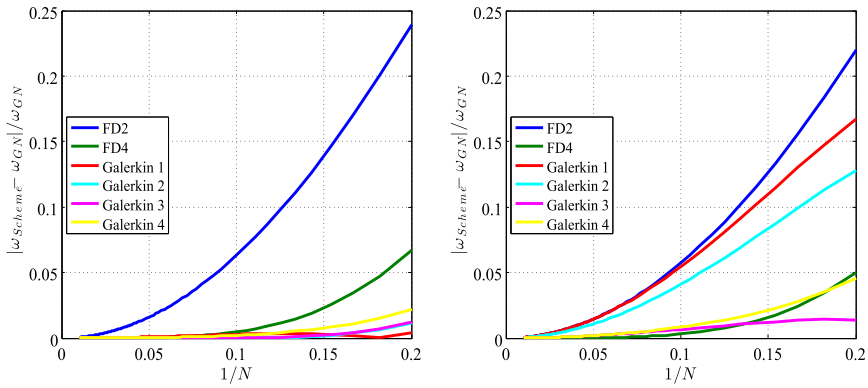

Fig. 3. Dispersion error of the Galerkin scheme for $kh_0 = 0.5$ (left) and $kh_0 = 2.5$ (right): impact of lumping strategy.

equivalently to shallow and deep waters) respectively, and plotted against the inverse of the number of nodes per wavelength N. The relative errors of the FD2 and FD4 finite difference schemes are also reported as a reference (see appendix for detailed expressions). The pictures show that the centered Galerkin scheme provides a dispersion error which is comparable or better that the fourth order finite difference method.

In section 3.2 we mentioned some implementation choices associated to the finite element solution of the elliptic problem (9). These boil down to the type of quadrature used to evaluate some of the integrals, or, in other words, to the use of mass lumping for the mass matrices appearing in equations (11), (17) and (18). The first two, in particular, influence the form of the $\tilde{\Phi}_{LIN}$ injected in the hyperbolic component. We have studied the impact of this choice with interesting results. Four possibilities exist, for which explicit calculations are provided in the appendix:

1. mass lumping is performed in both (11) and (17), in which case the elliptic solver is exactly the same obtained with the FD2 method;
2. mass lumping is only performed in the computation of the auxiliary variable (17), and not in (11). In this case, the elliptic system is not identical to the FD2 one, however the third order derivative formula obtained is exactly the same as the one used in FD2;
3. no mass lumping is performed for the auxiliary variable (17), while (11) is lumped. In this case, the elliptic system is the same as the FD2 one, however, its right hand side contains an approximation of the third order derivatives obtained starting from an L^2 projection of the gradients of the free surface;
4. no mass lumping is performed, leading to the first in (48).

The differences between these four cases are visualized in Fig. 3 for the continuous Galerkin scheme, showing that in deep waters the first and second configurations provide a considerable increase in error. This clearly means that the most relevant parameter is the approximation of the third order derivative. It appears from the results that the use of an improved approximation of the free surface gradient in the third order derivatives is the key element to reduce the dispersion error. In particular, the configurations 1 and 2 provide errors of the same magnitudes as the FD2 scheme, despite the fact that the hyperbolic phase, and part of the elliptic phase, are not the same. These are precisely the cases in which the approximation of the third order operator is the same as in FD2.

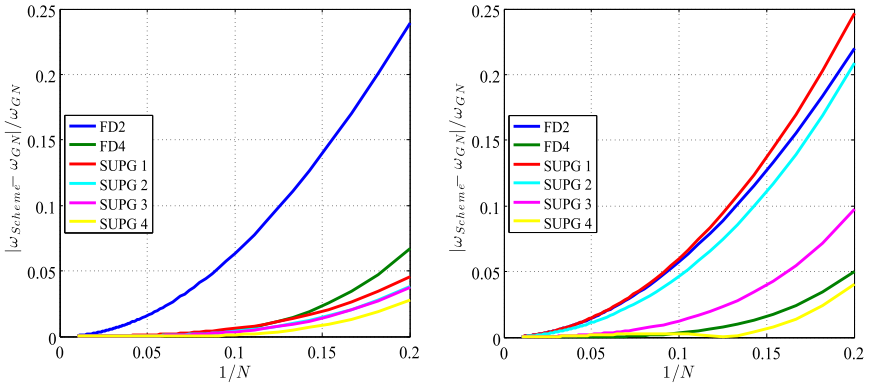

Fig. 4. Dispersion error of the SUPG scheme for $kh_0 = 0.5$ (left) and the $kh_0 = 2.5$ (right): impact of lumping strategy.

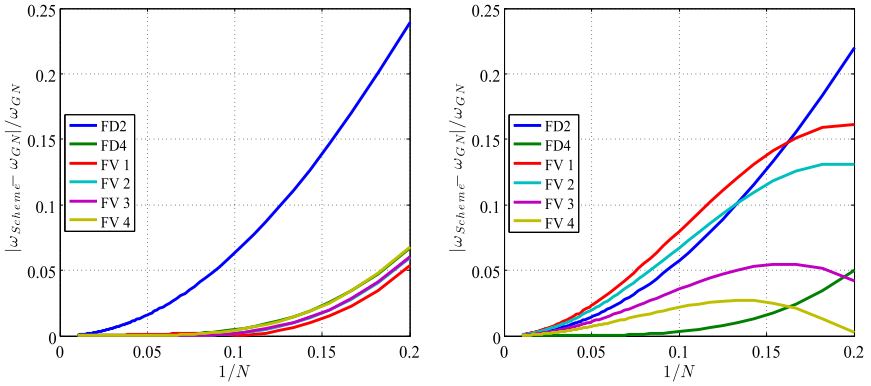

Fig. 5. Dispersion error for the FV scheme for $kh_0 = 0.5$ (left) and the $kh_0 = 2.5$ (right): impact of lumping strategy.

5.1.2. SUPG scheme

We repeat the analysis for the upwind stabilized finite element scheme (SUPG). We refer to the appendix for details and analytical expressions. Please, note that a system similar to (48)–(49) has to be analyzed and, in particular, that the first equation of this system is exactly equation (48) itself.

In Fig. 4, we visualize the impact of the mass lumping strategy on the dispersion error, as done for the un-stabilized method. Also in this case, for short waves/deep waters the largest errors are obtained whenever the third order derivatives are approximated with the simple FD2 formula (cases 1 and 2). In the other two cases, involving an improved treatment of this term, we obtain errors comparable or even smaller than those of the non-stabilized method, confirming the results already obtained in [60].

5.1.3. Finite volume

We repeat the exercise for the hybrid Galerkin-FV scheme of section 3.3, reporting the main findings in Fig. 5. Once more, the critical element to obtain low errors in deeper waters is the approximation of the third order derivative. The use of the FD2 approximation for this term (cases 1 and 2) provides error levels comparable to those of the FD2 scheme. The improvement in the approximation of the nodal gradient (17) leads to a reduction of the error of a factor three or four, providing errors close to those of the FD4 method. The best results are obtained in this case when no mass lumping is performed.

5.1.4. Time continuous analysis: summary

This analysis has allowed to highlight the following results. First, the behavior of the schemes is quite similar, despite the different treatment of the hyperbolic part. It appears that the treatment of the third order derivatives is very important, and in particular that the use of exact quadrature in the L^2 projection defining the auxiliary variable (17) is fundamental to reduce the error for deeper water/shorter waves. When no lumping is performed, the errors are similar or smaller than those provided by fourth order finite differences.

Finally, these similarities allow to provide a general recipe for the elliptic solver, as, for all the methods involved, the choice of the approach 4 allows to reduce the dispersion errors to those of the FD4 scheme or below. A summary of the resulting error curves is reported in Fig. 6 confirming the above observations.

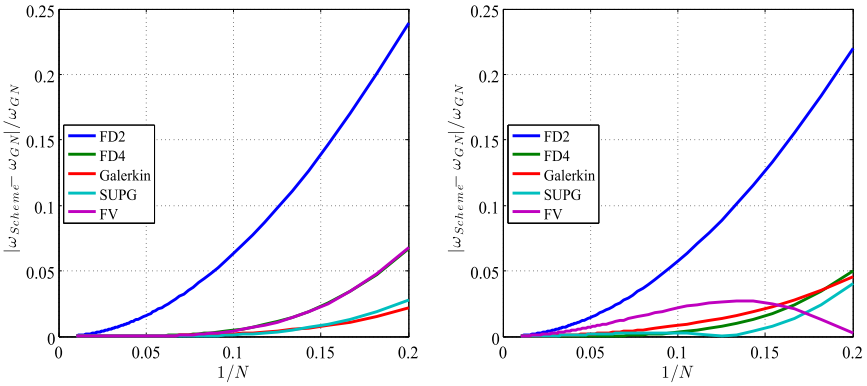

Fig. 6. Dispersion error of FD2, FD4, Galerkin, SUPG, and FV schemes. Left: $kh_0 = 0.5$. Right: $kh_0 = 2.5$.

5.2. Space continuous error analysis

For completeness, we include the error analysis of the time schemes, w.r.t. dispersion and amplification rate in the linearized case. As before, we start by injecting the Fourier mode $W = \hat{W}(t)e^{jkx}$. Setting $c^2 = gh_0$, and $\mu = kh_0$, we can use now (46) to deduce

$$\phi = jkc^2 \frac{\mu^2/3}{1+\alpha\mu^2/3}\eta$$

so that the Fourier symbol for the last in (47) is

$$c^2\eta_x - \phi = jkc^2(1 - \frac{\mu^2/3}{1+\alpha\mu^2/3})\eta$$

The last expression, however, is also obtained as from the equivalent PDE

$$q_t + a^2\eta_x = 0\,,$$

having set $\partial q = h\partial u$, and

$$a = a(\mu) = c\sqrt{1 - \frac{\mu^2/3}{1+\alpha\mu^2/3}}. \tag{50}$$

Indeed, relation (7) of the Green–Naghdi system is also obtained from the "dispersion equivalent system"

$$\eta_t + q_x = 0$$
$$q_t + a^2(\mu)\,\eta_x = 0$$

providing the phase relation $\omega^2 = k^2a^2$, which reduces to (7) with definition (50). Here the stability condition $\alpha \geq 1$ is necessary for the well-posedness of the analogy. The analysis of the time discretization will thus be performed on the ordinary differential system obtained from these equivalent PDEs, namely

$$\frac{d}{dt}\mathbf{U} = \mathcal{L}(\mathbf{U}) = -jk\begin{pmatrix} q \\ a^2\eta \end{pmatrix} = -jkA\mathbf{U}$$

having set $\mathbf{U} = (\eta,\ q)^t$. The rest is quite classical (cf. [35]): A admits the eigenvalue decomposition:

$$A = \begin{pmatrix} 0 & 1 \\ a^2 & 0 \end{pmatrix} = \underbrace{\begin{pmatrix} 1 & 1 \\ -a & a \end{pmatrix}}_{R_A} \begin{pmatrix} -a & 0 \\ 0 & a \end{pmatrix} \underbrace{\frac{1}{2}\begin{pmatrix} 1 & -1/a \\ 1 & 1/a \end{pmatrix}}_{L_A}$$

so we can analyze the schemes for the scalar (characteristic) ODE

$$\dot{w} + \lambda(\mu)w = 0$$

with $\lambda(\mu) = \pm jka(\mu)$. The analysis follows the same lines as in the time continuous case: a mode of the type $w_0e^{j\nu t}$ is injected in the time discretized form of the last ODE; this leads to an algebraic equation for the complex amplification rate ν which is solved numerically. The qualitative behavior obtained are displayed in Fig. 7. The three methods provide a

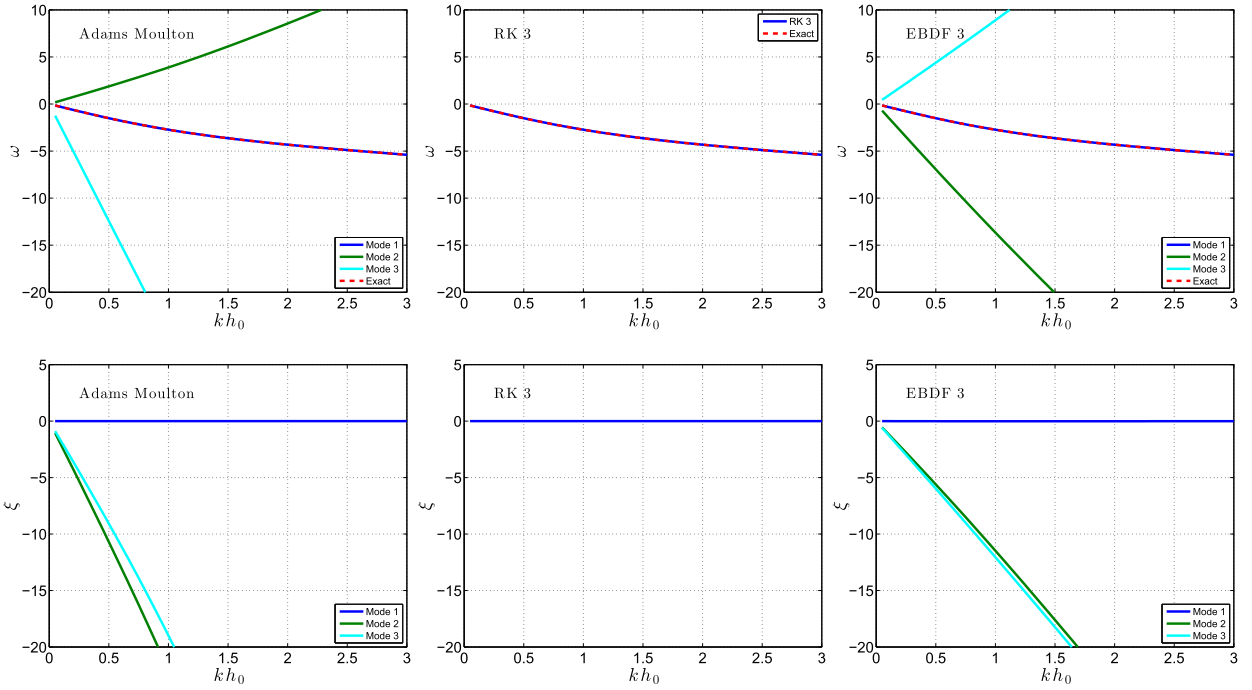

Fig. 7. Dispersion error of the time discretizations: overview. Left: AM scheme. Middle: RK3 scheme. Right: eBDf3 scheme.

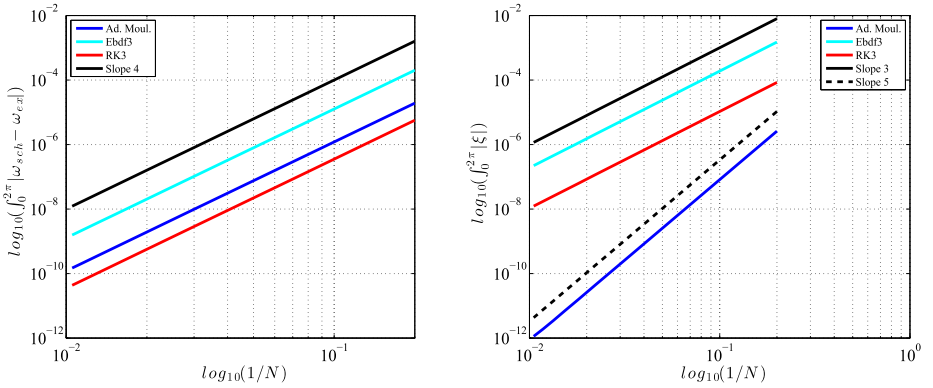

Fig. 8. Error analysis of the time discretizations: phase (left) ad amplification rate (right).

discrete mode approximating very well the linear phase relation of the Green–Naghdi equations, with a very small amount of dissipation. As expected, the multistep methods also provide two unphysical modes, which however present an extremely strong damping rate.

To provide more quantitative information we consider the convergence of the error in function of the number of points per wavelength obtained via the relations $N = \lambda/\Delta x$, $\lambda k = 2\pi$ and the CFL condition $\Delta t = \mathrm{CFL}\Delta x/c$, which lead to

$$k\Delta t = \frac{\mathrm{CFL}}{c}\frac{2\pi}{N}$$

with the maximum allowed CFL used for each scheme. The results obtained are summarized in Fig. 8. Note that for the multistep schemes, only the physical root is in the analysis. From the figure we can see that the errors of the third order RK3 and eBDf3 methods have a dominant component which is acting on the amplification rate, while the dispersion relation itself is of fourth order, making these schemes very accurate for propagation purposes. Concerning the AM method, we see that the error is dominated by the dispersion component, which again is of fourth order. The error on the amplification rate is found, instead, to be of order five. This shows that the third order methods considered provide comparable accuracy to the fourth order AM scheme. The choice between these methods may be done based on other considerations: boundedness preservation properties (known for the RK method, and for eBDF in the linear case), effective CFL (favoring the AM method), ease of generalization to higher orders, etc.

6. Embedding wave breaking

Wave breaking is an important modelling issue in near-shore environments. It dissipates wave energy through the generation of turbulence, including substantial air entrainment. As wave shoal, wave fronts become steeper and steeper, until wave's crest overturns. Depth averaged equations are unable to describe this phenomenon and an additional physical closure for wave breaking is necessary to simulate the breaking process numerically. The closure model is composed of two main elements: a trigger mechanism related to the initiation and possibly the termination of the breaking process; an energy dissipation mechanism. In this work, as in [72,37,6], the breaking dissipation is included by reverting locally to the non-linear shallow water (NLSW) equations and letting breaking fronts converge into moving bores or hydraulic jumps. The total energy dissipation through these features is used as a model for wave breaking dissipation. Such an approach leads to hybrid models and has gained attention by several researchers in the past few years, please refer to [13,73,74,36,67,63,56,72,76].

In the solution procedure proposed here, this can be embedded quite simply by setting ϕ to zero in (10). However, we will also test a tighter coupling of the hyperbolic and elliptic phases, by taking into account the presence of breaking regions also in the latter. More details concerning the detection and triggering of the breaking model and on the coupling between Green–Naghdi and NLSW equations are discussed hereafter.

6.1. Breaking front detection

As a trigger mechanism to determine the initiation and termination of a breaking process, we use the combination of physical criteria presented in [37]:

- the surface variation criterion: $\partial_t \eta \geq \gamma \sqrt{gh}$, with $\gamma \in [0.3,\ 0.65]$ depending on the type of breaking;
- the local slope angle criterion: $\|\nabla \eta\|_2 \geq \tan(\phi_c)$, where ϕ_c is the critical front slope at breaking, and $\phi_c \in [14^o,\ 33^o]$ depending on the type of breaking.

The first criterion flags for breaking when $\partial_t \eta$ is positive, as breaking starts on the front face of the wave and has the advantage that can be easily calculated during the running of the code. The second criterion acts complementary to the first one and is based on the critical front slope approach [65,68]. This allows to flag steady hydraulic jumps, while the first is more effective for moving fronts.

As discussed in [37,72], the different breaking waves are distinguished, and each one is processed individually. In particular, for each front one computes peak and trough depths (h_{peak} and h_{trough} respectively). If the critical Froude number, defined by

$$\text{Fr} = \sqrt{\frac{-1 + (1 + 2h_{\text{peak}}/h_{\text{trough}})^2}{8}},$$

is larger than a certain threshold, typically $\text{Fr}_c \approx 1.3$, then a breaking region is defined, centered around the point of maximum slope and of width $l_{\text{NLSW}} \approx 7.5(h_{\text{peak}} - h_{\text{trough}})$. All the nodes within this region are breaking nodes. For breaking nodes, the shallow water equations are solved. The modifications to the numerical model made to achieve this coupling are discussed in the next paragraph. More details on wave breaking detection can be found in [37,72] and references therein.

6.2. Numerical treatment of breaking regions

In the region flagged as breaking, the flow quantities are evolved using the shallow water equations. We will compare in our results two different approaches:

1. Simply neglect the terms related to ϕ in the spatial discretization. For a breaking node i, this means setting $\overline{\mathbf{\Phi}}_i = 0$ in (19), or (33). In this case, the two phases of the discretization (elliptic and hyperbolic) are completely independent of one another. In particular, only the hyperbolic phase is aware of the breaking process;
2. To have a tighter coupling between the two phases, and hopefully a smoother transition, the breaking condition is embedded in the elliptic phase as a sort of Dirichlet boundary condition. In particular, for a breaking node i the line of the matrix issuing form the finite element discretization discussed in section 3.2 is replaced by $\delta_{ij}\Delta x$, δ_{ij} denoting Kroenecker's δ, while the right hand side is set to zero. The elliptic problem being second order, the discrete solution for ϕ is now expected to go to zero in breaking nodes trying to keep also the continuity of its first derivative. As the source term $\overline{\mathbf{\Phi}}$ is kept into the discretization, and as it involves an average of neighboring values of ϕ, a smoother transition may be expected.

In both cases, the nonlinear limiters involved in the discretizations are turned on only if the nodes are breaking. In other words, in non-breaking regions we set $\psi = 1$ in both (21) and (32).

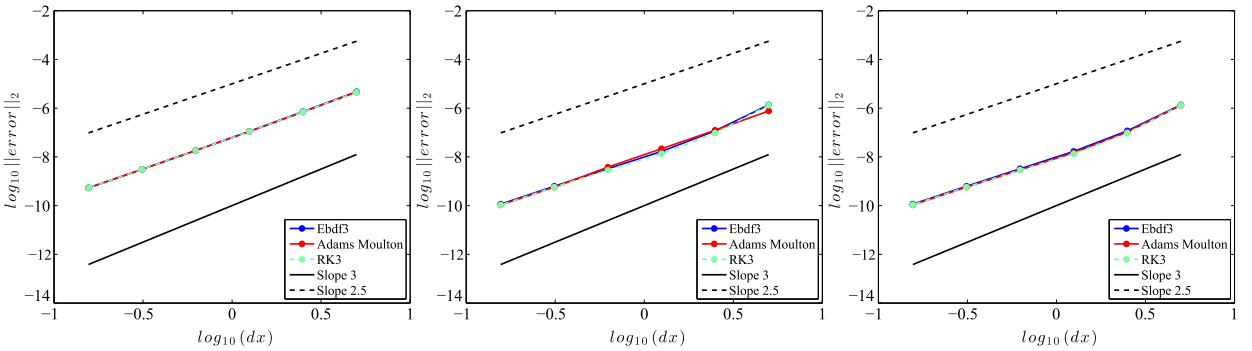

Fig. 9. Convergence rates for the FV scheme (left) the SUPG scheme (center) and the Galerkin scheme (right).

7. Numerical tests and results

7.1. Space–time grid convergence

We perform a convergence analysis w.r.t. space and time step size. The physical case considered is the propagation of a solitary wave over a flat bed, with depth $h_0 = 10$ m, and with $\epsilon = 0.2$. The domain is of 2000 m, [0, 2000] and the initial wave was placed in $x_0 = 1000$ m. For this case, an analytical solution is available. The test case is performed on a set of six meshes with $dx = 5,\ 2.5,\ 1.25,\ 0.625,\ 0.3125,\ 0.1562$ m, and with corresponding time step sizes refined according to (35), with CFL$\approx$ 0.2. At $T = 1$ s the relative error $E_{L_2}(h) = \|h_{num} - h_{ex}\|_2 / \|h_{ex}\|_2$ on the total water depth is computed, where h_{num} is the numerical solution and h_{ex} is the analytical one.

The convergence of the L^2 error is plotted in Fig. 9, where the slopes 2.5 and 3 are also plotted for reference. Similar behaviors are observed with other norms. The slopes obtained from the error reveal convergence rates in between 2.5 and 3 for all the combinations, showing that the dominant component of the error is the one related to the spatial discretization.

7.2. Periodic wave propagation over a submerged bar

The next test case is the periodic wave propagation over a bar. The classical tests of Beji and Battjes [8] examine sinusoidal wave propagation over a submerged bar as to investigate the frequency dispersion characteristics and nonlinear interaction of complex wave propagation phenomena. The experiments were conducted in a 37.7 m long, 0.8 m wide, and 0.75 m high wave flume. A hydraulically driven, piston-type random wave generator was located at the left side of the flume and a 1 : 25 plane beach with coarse material was placed at the right side to serve as a wave absorber. The submerged trapezoidal bar was 0.3 m high with front slope of 1 : 20 and lee slope of 1 : 10 separated by a level plateau 2 m in length. For the numerical test case, the wave-making internal source function is placed at $x = 0$ m and the dimension of the computational domain is set to $x \in [-10, 29$ m$]$. Sponge layer widths are set to $L_s = 5$ m at both ends of the computational domain. For the computation $dx = 0.04$ m and the CFL number used is equal to 0.2.

Case (a): First we consider the test case with $A = 0.01$ m incident wave amplitude and $T = 2.02$ s wave period. The water depth parameter is $kh_0 \approx 0.67$ with depth to wavelength ratio $h_0/L = 0.11$ m. The propagating waves shoal along the front slope of the bar causing the growth of the wave amplitude and the surface profile to become asymmetric. In the back slope the waves break up into independent waves which travel at their own speed. Fig. 10 presents the comparison between experimental data and numerical ones, produced using the FV scheme, recorded in wave gauges for all the time schemes used in this work. Figs. 11 and 12 present the same for the Galerkin and the SUPG schemes respectively. We must mention that the wave signals have been phase calibrated according to gauge 4. For brevity we only consider gauge 4 placed at the toe of the bar, gauge 7 placed before the plateau of the bar, gauge 8 placed on the top of the bar and gauge 10 placed after the bar.

We can observe that the three scheme produce same results for the gauges before and on the plateau of the bar while there is a slight modification for the gauge in the lee side of the bar. In this region the water depth parameter kh increases rapidly so it is expected form Fig. 6 that the FV scheme produces less accurate results since the dispersion error is higher as k grows.

Case (b): In this case wave breaking is expected to occur at the end of the first slope and after the shoaling of the waves. The waves height is of 0.054 m and the wave period is $T = 2.5$ s, that corresponds to the water depth parameter $kh_0 \approx 0.52$, with depth to wavelength ratio of $h/L = 0.0835$. The value of the surface breaking criterion γ, for the wave breaking mechanism, is set to 0.3. We muse denote that for the numerical treatment of the wave breaking (in all the test cases), we use the second approach described in section 6.2. A discussion on the topic will follow. The numerical results along with the experimental data are recorded in four wave gauges (1 to 4) which were placed at $x = 6, 12, 13$ and 14 m respectively. They are all presented in Figs. 13 and 14 for the FV and the SUPG schemes respectively.

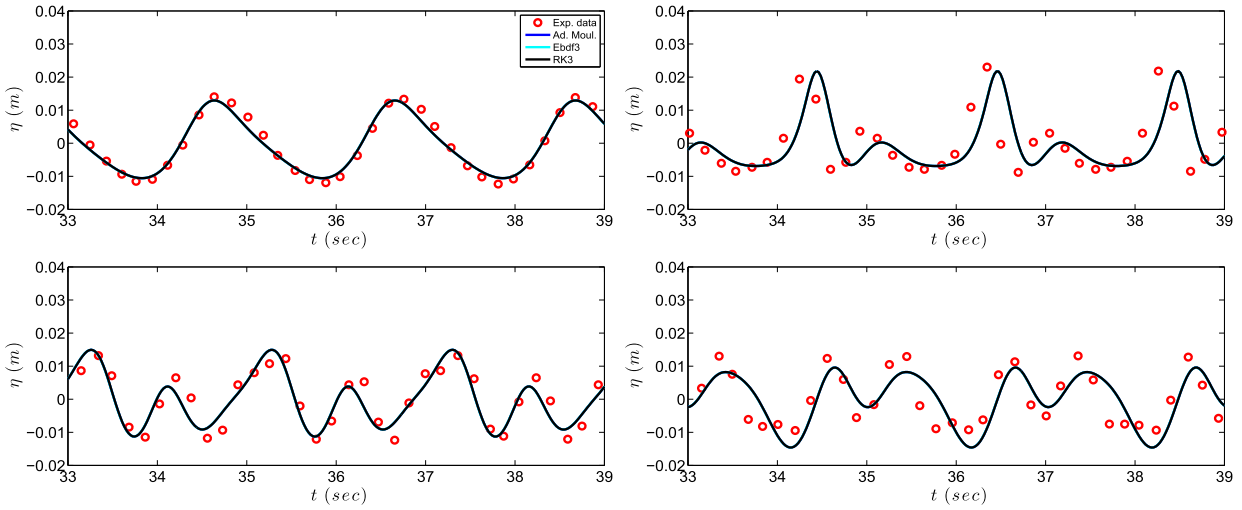

Fig. 10. Time series of surface elevation, for the FV scheme, at wave gauges 4, 7 (up) 8, 10 (down) for periodic wave propagation over a bar.

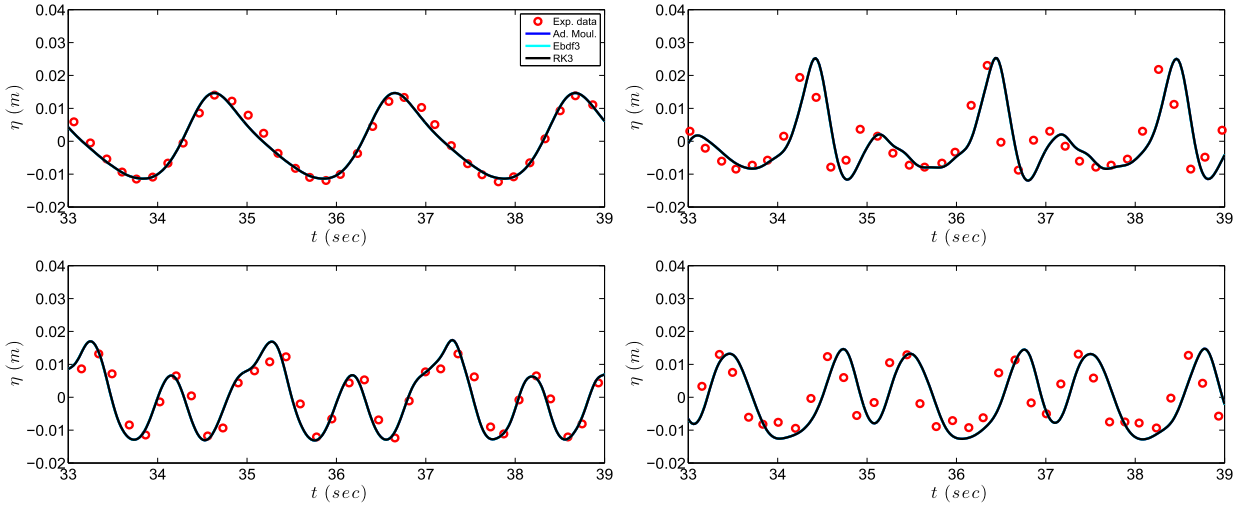

Fig. 11. Time series of surface elevation, for the Galerkin scheme, at wave gauges 4, 7 (up) 8, 10 (down) for periodic wave propagation over a bar.

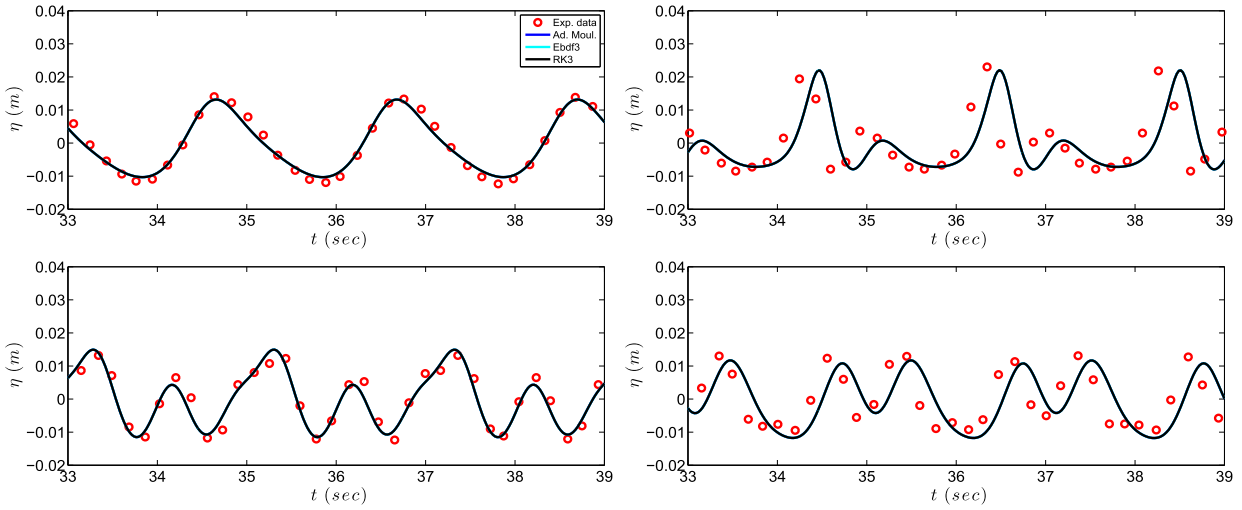

Fig. 12. Time series of surface elevation, for the SUPG scheme, at wave gauges 4, 7 (up) 8, 10 (down) for periodic wave propagation over a bar.

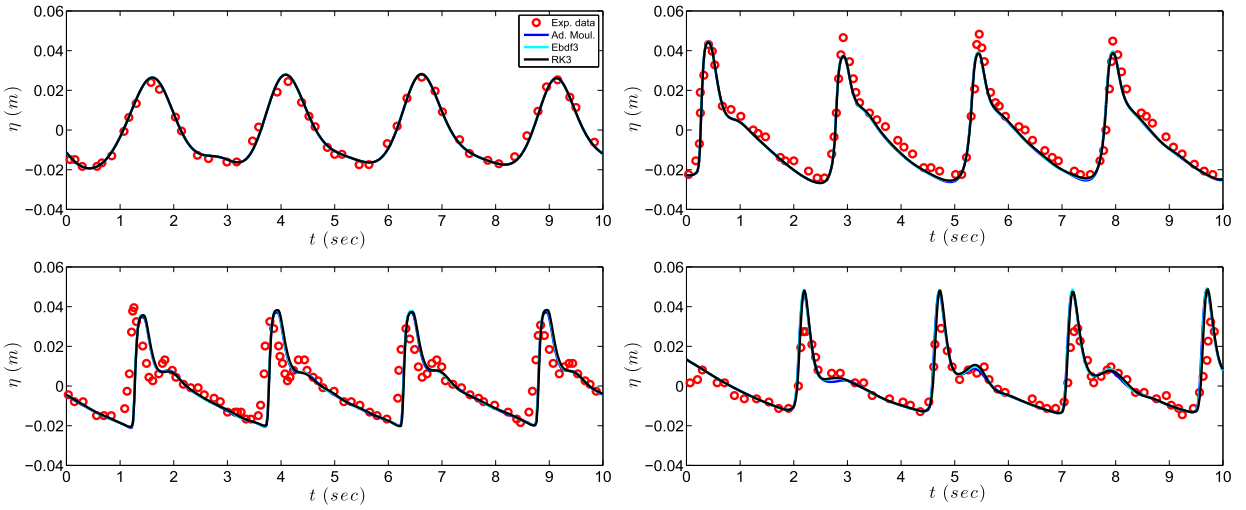

Fig. 13. Time series of surface elevation, for FV scheme, at wave gauges for periodic wave propagation over a bar.

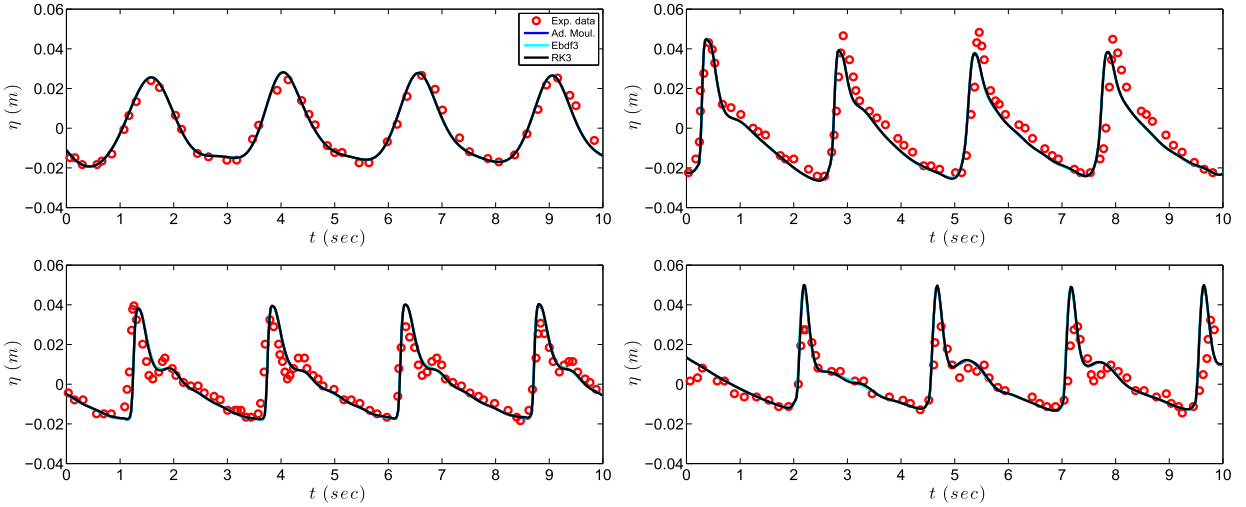

Fig. 14. Time series of surface elevation, for FE scheme, at wave gauges for periodic wave propagation over a bar.

The wave shape is well-reproduced for all wave gauges. As expected the waves shoal along the front slope, since nonlinear effects cause the waves propagating along this slope to steepen and broke at the beginning of the bar crest. Breaking is classified as plunging. Bound higher harmonics are developed along the front slope, which are then released from the carrier frequency on the lee side of the bar as the water depth parameter kh increases rapidly. Figs. 15 and 16 illustrate the wave-by-wave treatment and the l_{NLSW} area along the centerline for FV and SUPG schemes respectively, at different time instances (covering roughly one wave period). The time scheme used for both models was Adams Moulton but similar results can be obtained using the other time schemes. The onset of breaking is correctly predicted for both schemes, close to the beginning of the bar crest and continues along the flat of the bar leading to a wave height decay. We can observe that during the breaking process the SUPG scheme is more diffusive leading to a slightly earlier termination of the procedure and after that a small amplification of the wave height compared to the FV scheme. Different particularization for the breaking model maybe needed for different numerical models but this study is beyond the purpose of this work.

7.3. Solitary wave run-up on a plane beach

As to verify and validate our implementations, we use one of the most intensively studied problems in long-wave modeling, the solitary wave-run up on a plane beach. Synolakis [70] carried out laboratory experiments for incident solitary waves of multiple relative amplitudes, in order to study propagation, breaking and run-up over a planar beach with a slope 1:19.85. Detailed description of the test case, along with the initial conditions, can be found for example in [70,11,74,63,24] among many others. The incident wave height used in this work is $A/h = 0.28$ with $h = 1$ m. This wave breaks strongly

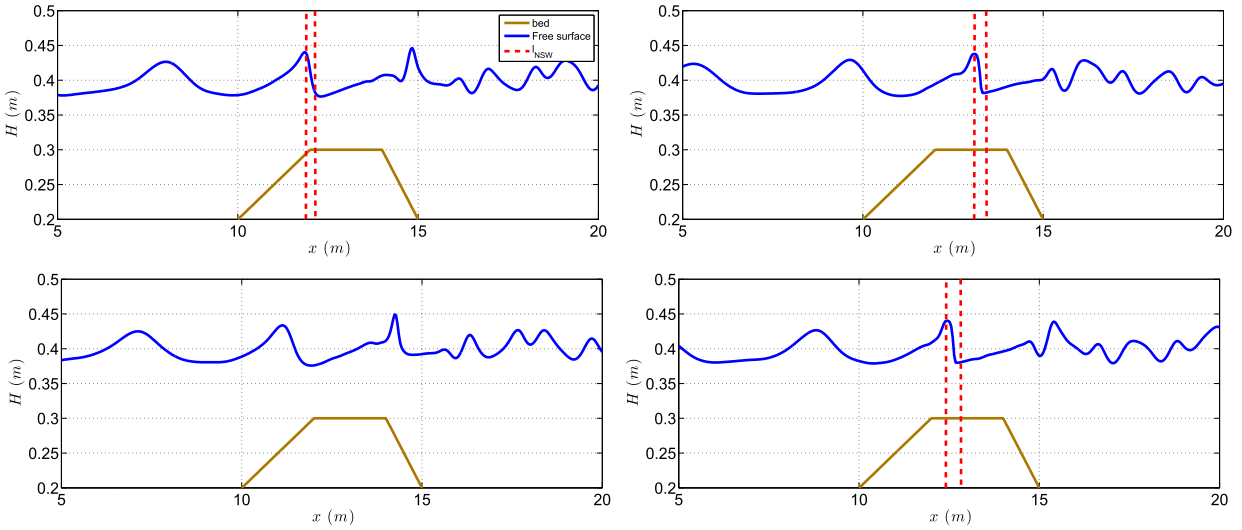

Fig. 15. Spatial snapshots, for FV scheme, along the centerline of regular waves breaking over a bar with the flow between two consecutive vertical lines governed by the NSW equations.

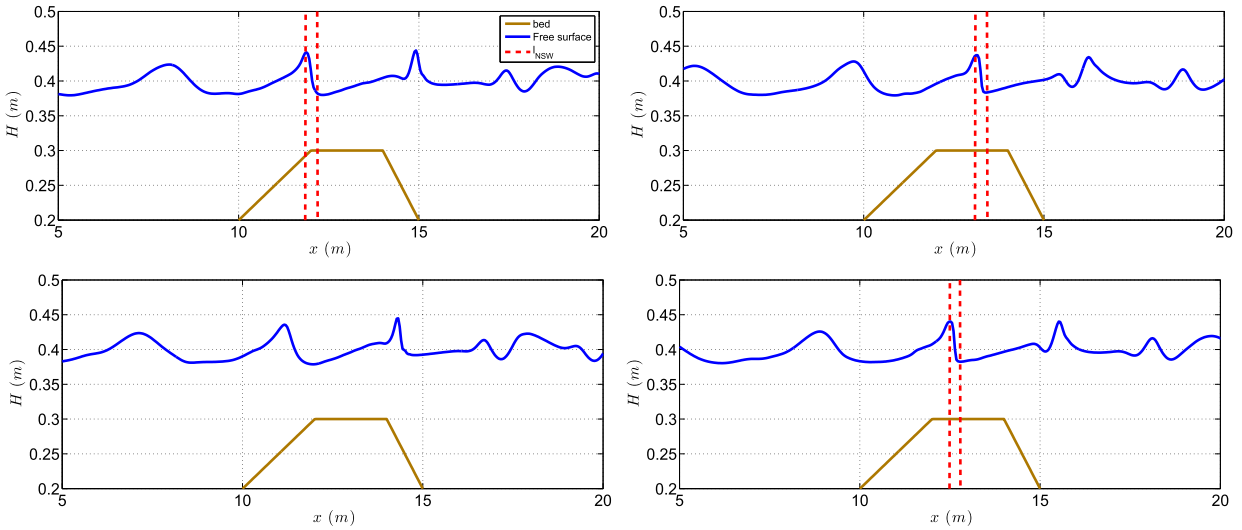

Fig. 16. Spatial snapshots, for SUPG scheme, along the centerline of regular waves breaking over a bar with the flow between two consecutive vertical lines governed by the NSW equations.

both in the run-up and the run-down phases of the motion. The computational domain used is $x \in [-20,\ 100\ \text{m}]$ with $dx = 0.05$ m. The CFL number is set equal to 0.2, a sponge layer is applied offshore with length $L_s = 5$ m and γ is set equal to 0.6. Finally, a Manning coefficient of $n_m = 0.01$ is used to define the glass surface roughness used in the experiments.

We perform this test case using all the time schemes described up to now. Like the periodic wave propagation over a bar, we obtain the same results for the different time schemes. For brevity, only two snapshots of the comparison are presented in Fig. 18. Since we show that all the time schemes used up to now lead us to the same results, from now on, the presented results will use Adams Moulton time scheme unless otherwise said. Of course the choice of the above time schemes is not restricted and any time scheme of order greater than three can be used. Fig. 17 compares the measured surface profiles and the numerical model's results on different non-dimensional times. Blue line denotes the numerical results produced by the FV scheme, green dotted line the results given by the SUPG scheme and red circles denote the experimental data.

Until time $t\sqrt{g/h} = 10$ the solitary propagates to the shore and the two models produce, as expected, identical results since wave breaking hasn't started yet. The experimental wave, breaks around $t\sqrt{g/h} = 20$. The numerical solution is represented like a bore storing the water spilled from the breaking wave behind the front. A slight difference can be seen in the two solutions at time $t\sqrt{g/h} = 20$ which is due to the usage of two different limiters. SUPG scheme uses the smooth sensor limiter while FV scheme uses the min-mode limiter. Usage of different limiters produces different results in the wave breaking region but this study is beyond the scope of this work. At time $t\sqrt{g/h} = 25$ the bore collapses at the shore

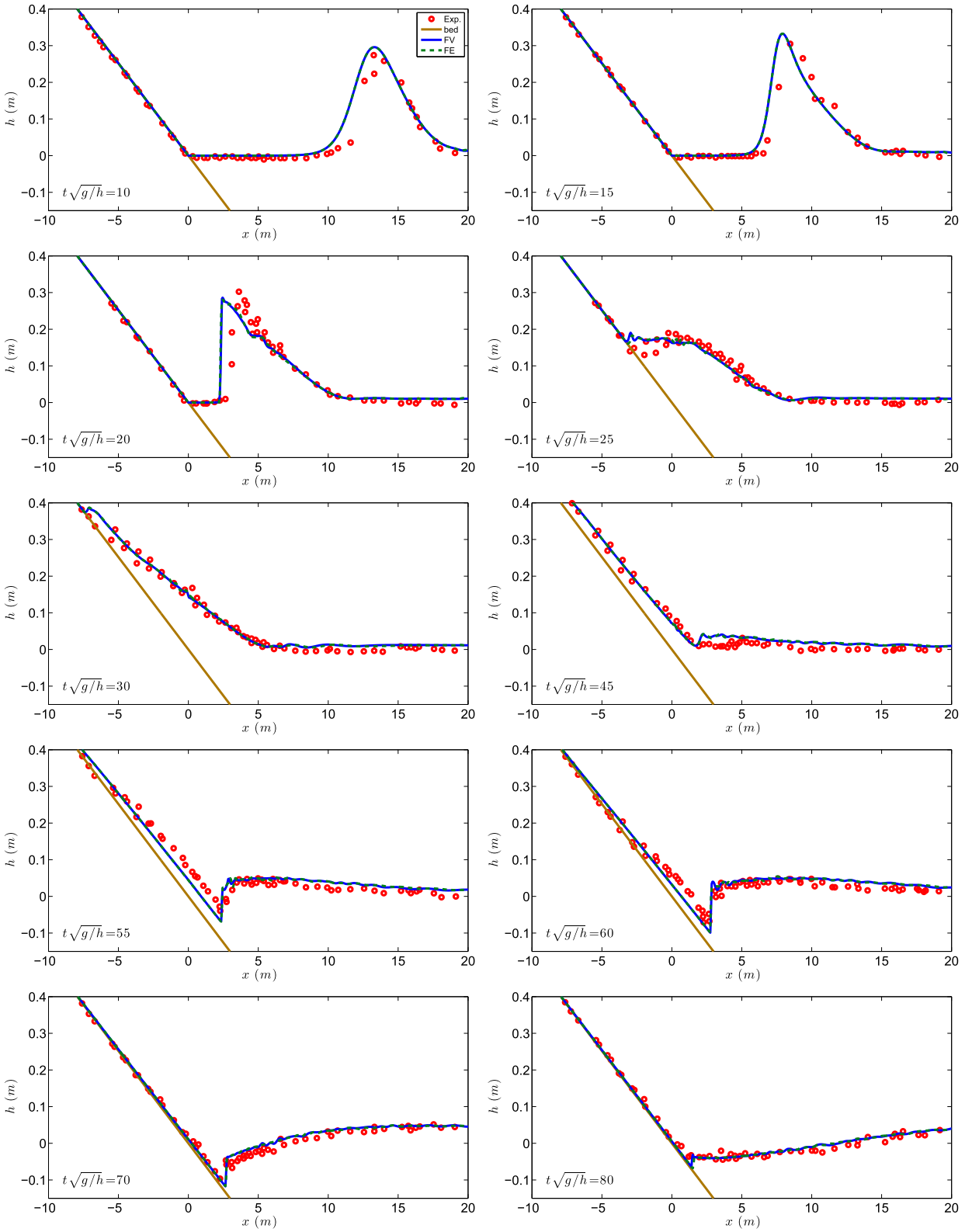

Fig. 17. Free surface elevation of solitary wave run-up on a plane beach for $A/h = 0.28$.

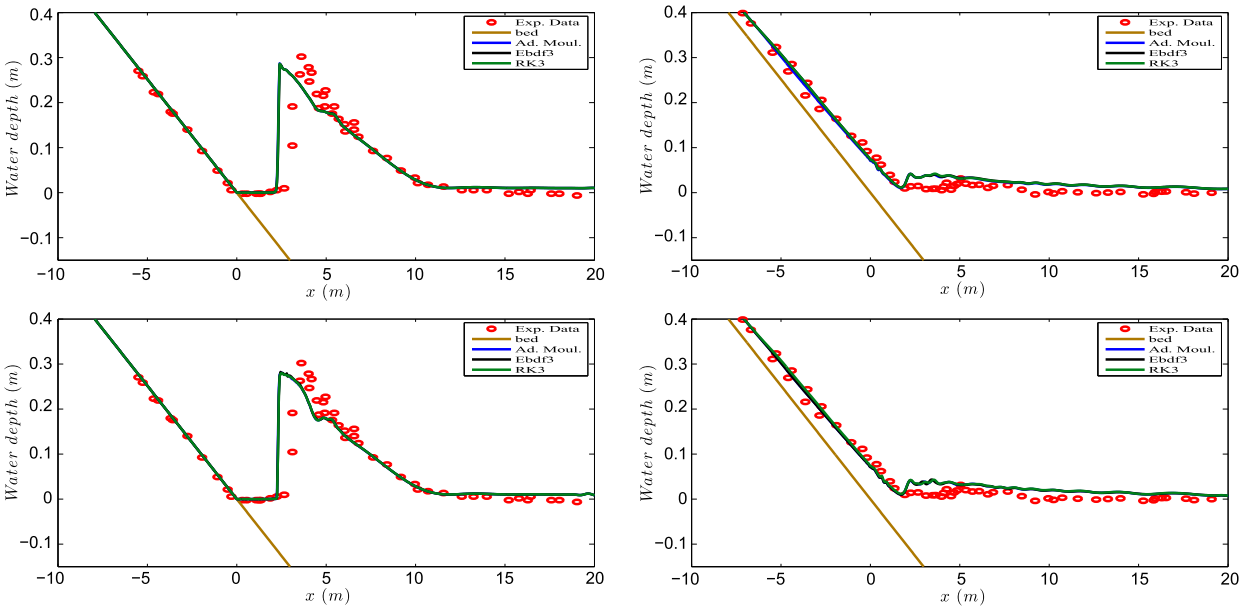

Fig. 18. Comparison of different time schemes on a solitary wave run-up on a plane beach, for the FV scheme (up) and the SUPG scheme (down).

and the results show really good agreement. After that the wave starts to run-up. The time of maximum run-up occurs at $t\sqrt{g/h} = 45$. During the backwash a breaking wave is created at $t\sqrt{g/h} = 55$ near the still water level. The numerical solution is approximated as a hydraulic jump for both models which can be fully resolved since the breaking criterion recognizes it and the NLSW equations are used in this region.

7.4. Influence of mesh regularity

In order to assess the influence of mesh regularity on the results, we present some examples of computations on perturbed point distributions, obtained from uniform ones by displacing all the points by a factor of $\rho_i \Delta x$ (with ρ_i a random number such that $|\rho_i| \leq 0.2$, and with Δx the initial mesh size). For completeness we consider both a smooth case, and a non-smooth one.

The first test involves the interaction of two symmetric solitary waves in a flat frictionless channel. This head-on collision is characterized by the change of shape, along with a small phase-shift of the waves as a consequence of the nonlinearity and dispersion. We consider a channel 200 m long with $h_0 = 1$ m, and two solitary waves with an equal initial hight of $A/h_0 = 0.3$, initially centered at $x = 60$ m and $x = 140$ m. The computational parameters used are CFL value 0.2, number of nodes 4000 and domain $x \in [0,\ 200\ \text{m}]$.

Fig. 19 shows the surface profiles of the solitary waves in time $t = 5, 11$ and 17 s for the SUPG (up) and the FV model (down) respectively (virtually identical results are obtained with the Galerkin method). Each subfigure compares the numerical solutions obtained from the uniform and the non-uniform meshes. The waves initially propagate undisturbed until they collide. After the collision, as expected, the waves are transformed and a dispersive tail appears. The influence of mesh irregularity is clearly negligible.

As a non-smooth example, we repeat on a perturbed mesh the computation of a solitary wave run-up on a plane beach. The results obtained are shown in Fig. 20 for both the hybrid FV and SUPG methods, using the Adams–Moulton time integration. Comparing to the results of the previous section, we can again see that the influence of mesh regularity is very small, and perhaps the main impact of the irregularity is on the efficiency of the limiters implemented in detecting the shocks, especially for the SUPG scheme. This is clearly a topic for future improvement.

7.5. Solitary wave on a composite beach

One of the benchmark methods for tsunami model validation and verification according to the NOOA center for tsunami research is the problem the propagation of a solitary wave over a composite beach which simulates the Revere beach in Massachusetts. A physical model was constructed at the Coastal Engineering Research Center in Vicksburg, Mississippi by the U.S. Army Corps of Engineers. The configuration of the problem can be found in [42,71]. The setup of the problem is shown in Fig. 21. The wave gauges, where the time series of the surface elevation is examined, are placed at $x = 15.04$, 17.22, 19.04, 20.86, 22.33, 22.80 m. Two cases are implemented and tested in this work. The first one is the propagation and breaking of a solitary wave of $\epsilon = 0.3$ and the second one involves a solitary wave of higher non-linearity of $\epsilon = 0.7$. The computational domain used is of 27.23 m, $x \in [-5,\ 23.23]$, with the initial solitary placed at $x = 0$ m and $h_0 = 0.218$ m.

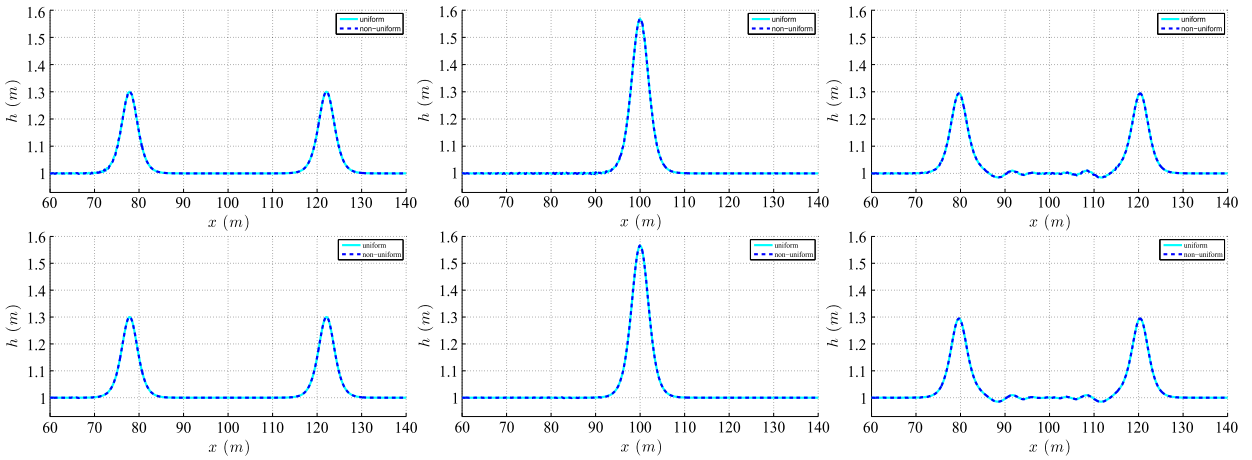

Fig. 19. Surface profiles of solitary waves at times $t = 5, 11, 17$ sec with A/h_0 propagate in opposite directions for SUPG (up) and FV (down) schemes.

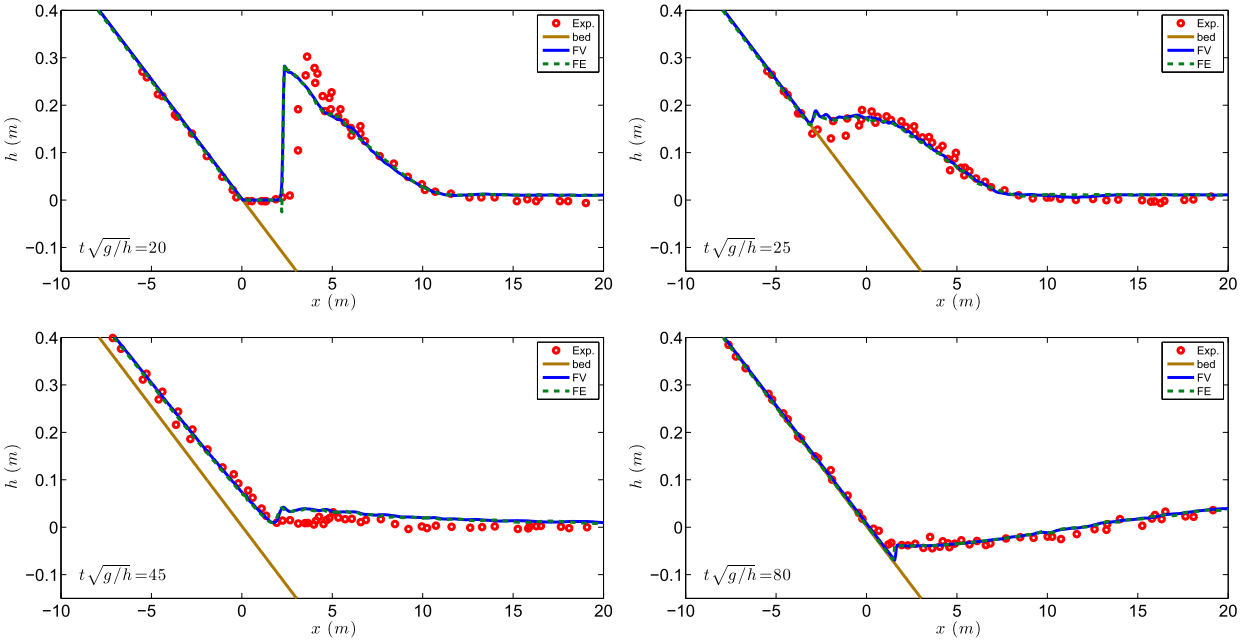

Fig. 20. Comparison on a solitary wave run-up on a plane beach, for the FV scheme and the SUPG scheme using a non-uniform mesh.

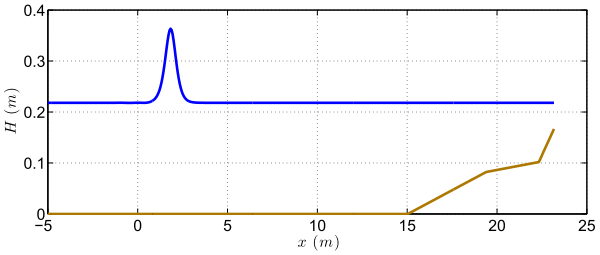

Fig. 21. Initial conditions of the solitary wave on a composite beach.

The CFL number is set to 0.2 and $dx = 0.046$ m. A sponge layer of 2 m is placed at the left boundary while a vertical wall is placed at the right boundary. For the surface variation criterion, γ is set equal to 0.6.

Fig. 22 shows the comparison between the experimental data (red circles) and the numerical results. Again, blue line denotes the numerical results produced by the FV scheme while green dotted line denotes the results given by the SUPG scheme. The solitary travels down the domain, shoals and break between the second and the third wave gauges. After

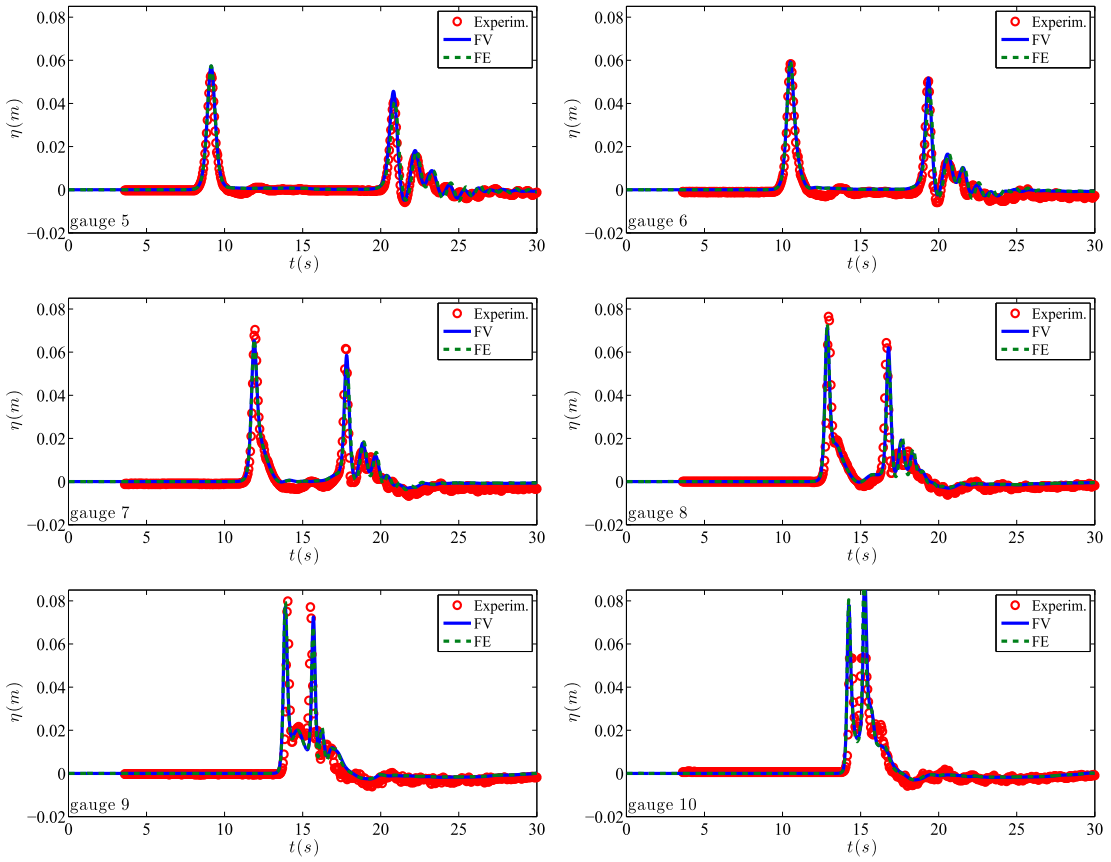

Fig. 22. Time series of the free surface elevation at the wave gauges for the solitary of non-linearity $\epsilon = 0.3$. (For interpretation of the references to color in this figure, the reader is referred to the web version of this article.)

breaking it continues to travel onshore until it hits the wall, reflects and starts to propagate offshore. We observe a very good match between the experimental data and the numerical results for almost all the wave gauges.

In Fig. 23 the numerical results along with the experimental data for the second case ($\epsilon = 0.7$) are presented. The solitary wave is highly non-linear and presents the same behavior. It breaks between the second and the third wave gauges, reflects on the wall and travels offshore. The numerical results are in agreement with the experimental data. We must notice that after the reflection of the solitary, the numerical results produced by the FV scheme are slightly ahead compared to the ones produced by the SUPG scheme and the experimental data.

7.6. Solitary wave propagation over a two-dimensional reef

The last experimental test case is on solitary wave transformations over an idealized fringing reef. It examines the model's capability in handling non-linear dispersive waves along with wave breaking and bore propagation. It was initially presented in [62] and the laboratory experiments have been carried out at the O.H. Hinsdale Wave Research Laboratory of Oregon state University from 2007 to 2009. The test includes a steep slope along with a reef crest in order to represent fringing reefs. The topography includes a fore reef slope of 1/12 a 0.2 m reef crest and a water depth $h_0 = 2.5$ m. The reef crest is then exposed by 6 cm and submerges the flat with $h = 0.14$ m. A solitary wave of 0.75 m high is used as an initial condition. The computational domain is $x \in [0, 83.7\text{ m}]$ with $dx = 0.1$ m. A CFL number of 0.2 is used, and $\gamma = 0.6$. Wall boundary conditions are placed at each boundary of the computational domain and, as suggested in [63], a Manning coefficient $n_m = 0.012\ \text{s/m}^{1/3}$ is used to define the roughness of the concrete surface of the reef. Experimental results for the free surface elevation were recorded at 14 wave gauges [62] along the centerline of the computational domain. Figs. 24 and 25 show the measured and computed wave profiles, for both schemes, as the numerical solitary wave propagates. For comparison purposes we also present the results obtained solving Nwogu's equations [54] with a FV scheme [36]. As the initially symmetric solitary wave propagates along the inclined bottom, it starts to shoal across the toe of the slope, at $x = 25.9$ m, and it begins to skew to the front. As expected [29], during the shoaling (at $t\sqrt{g/h} = 65$), Nwogu's equations slightly over predict the wave height. Higher amplitudes are also observed in the undular bore forming after the reflected waves overtop the reef again. This is clearly visible in the gauges in Fig. 26 and Fig. 27.

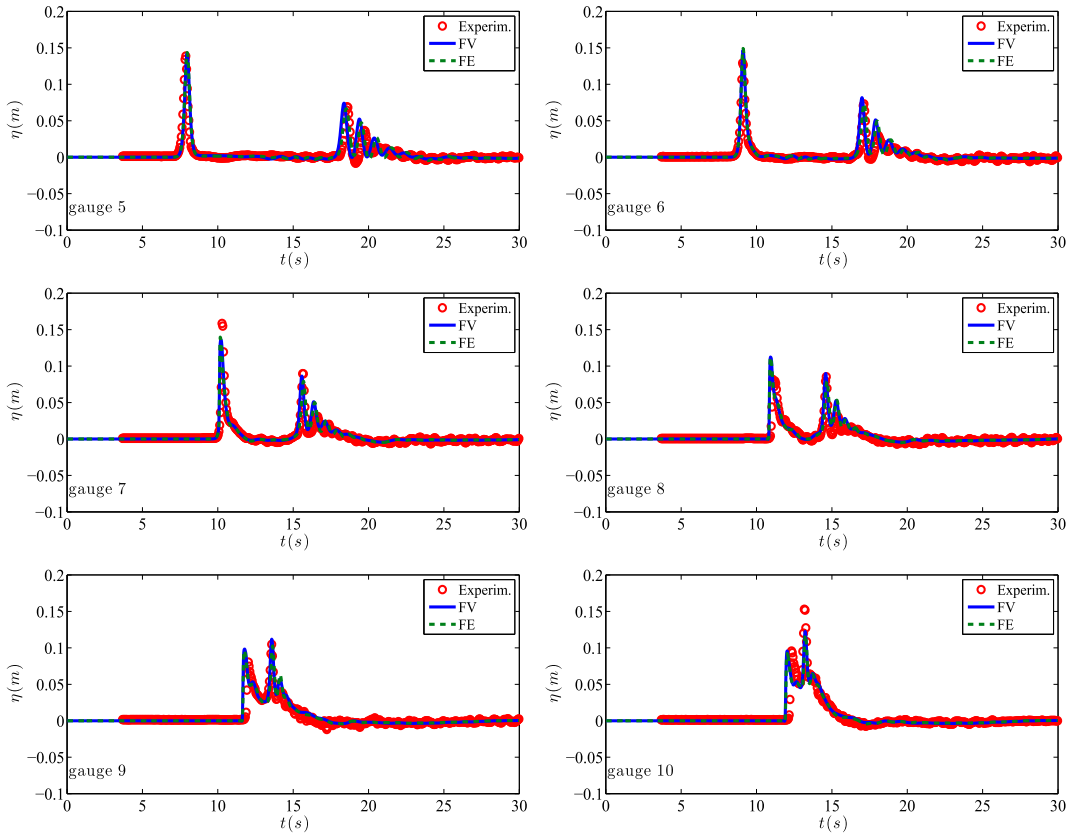

Fig. 23. Time series of the free surface elevation at the wave gauges for the solitary of non-linearity $\epsilon = 0.7$.

The wave begins to break as it approaches the reef, developing a plunging breaker on the top of the reef crest that collapses around $t = 68.5$ s. Both models (and all schemes) are mimicking the breaker as a collapsing bore that slightly underestimates the wave height, but conserved the total mass. The two models give identical results as the wave over tops the reef, deforming both a hydraulic jump and a downstream propagating bore. A difference can be observed in the approximation of the undular bore that forms after the reflection on the wall, over-top the reef and travels offshore. This indicates again that maybe different treatment of the breaking mechanism is needed for different numerical models, but this study is beyond the scope of this work.

7.7. Discussion on two different breaking formulations

As mentioned in section 5.2, in this work, we performed two different approaches concerning the implementation of wave breaking technique in both schemes. The first approach has the advantage that the elliptic and the hyperbolic parts are completely independent of one another and only the hyperbolic phase is aware of the breaking process. This makes it particular easy to implement in any hyperbolic scheme by simply using $\bar{\mathbf{\Phi}}$. In the second approach, we expect to achieve a smother transition between the two phases, but the breaking condition must be embedded in the elliptic part. In this section we use the two different wave breaking formulations in both schemes. We want to reveal the differences, if any, the limitations and advantages of each approach by performing test cases of different wave characteristics and breaking conditions.

The first test case performed is the solitary wave propagation over a plane beach. It was described in section 7.3. Fig. 28 shows the numerical results obtained from the two schemes and for both approaches and depicts the breaking procedure before the run-up of the wave. The left column corresponds to the FV scheme and the right column to the SUPG scheme. Each snapshot presents the free surface elevation and $\bar{\mathbf{\Phi}}$. We must mention that while for the FV scheme $\bar{\mathbf{\Phi}}_i$ contributes only to the momentum equation, this is not the case for the SUPG scheme in which $\bar{\mathbf{\Phi}}_i$ is coupled (see eq. (14)). For this reason and in all the results from now on, we present only the term contributed to the momentum equation. The numerical results obtained for both schemes are quite similar. We can observe that the first approach of wave breaking, in both schemes, tends to be slightly more oscillatory but without affecting the overall solution.

Fig. 29 describes the same problem but with a refined mesh of 4800 nodes. Here the oscillatory behavior of the first approach is revealed in both schemes but is more pronounced in the FV scheme. Oscillations are produced during breaking and due to the abrupt switching between the two formulations. They travel offshore and they affect the back of the wave.

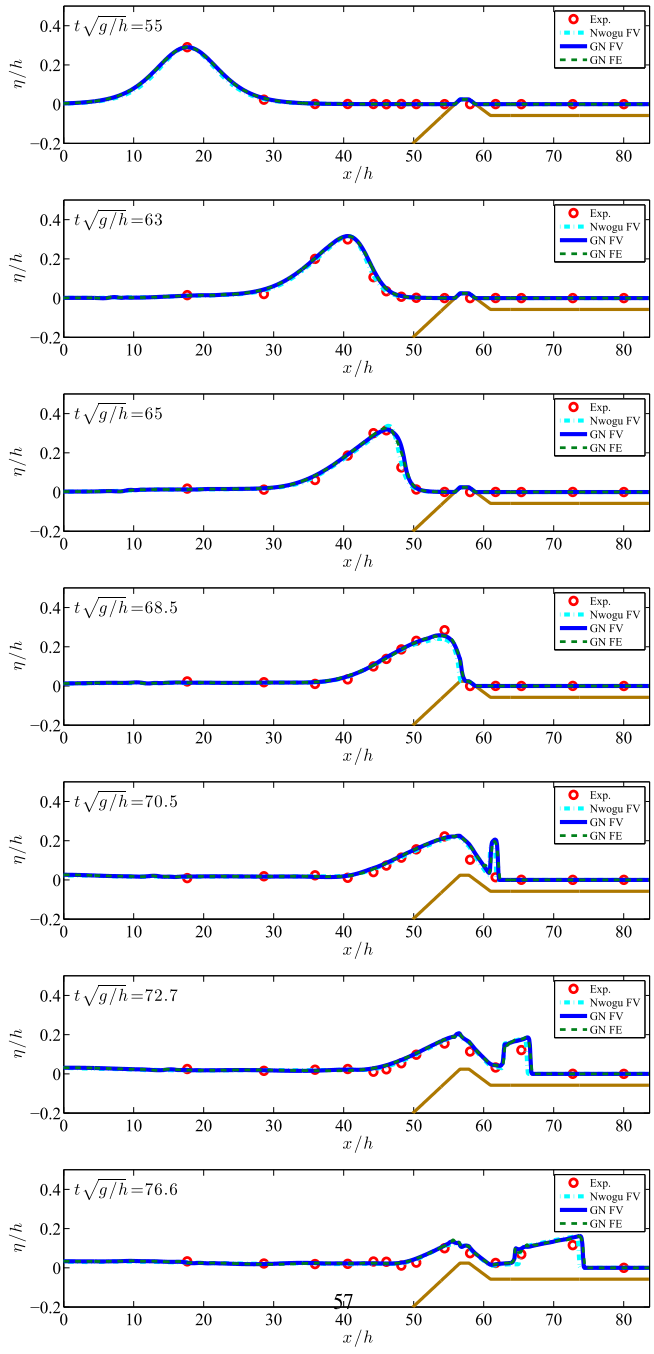

Fig. 24. Evolution of surface profiles and wave transformations over an exposed reef for $A/h = 0.3$ and $1/12$ slope.

We must mention that the SUPG scheme is more diffusive during breaking due to the different nature of the limiters used, compared to the FV scheme. Further research on the effects of the limiters during breaking is necessary. We observe that the more we refine the mesh the more oscillations on $\bar{\mathbf{\Phi}}$ are observed. These are introduced to the free surface elevation and eventually lead us to a non-acceptable solution.

Fig. 30 presents the numerical results for a solitary wave of $\epsilon = 0.5$ propagating in the same inclined topography as before. As expected the wave breaks in earlier time and once again the figures depict the strong breaking close to the shore. The same behavior as before is revealed.

On the contrast and for the wave propagation over a bar test case (see Fig. 31), we observe a different trend. While for the mesh of $dx = 0.04$ there are no big differences observed for the two approaches, for a refined mesh of 4000 nodes a phase

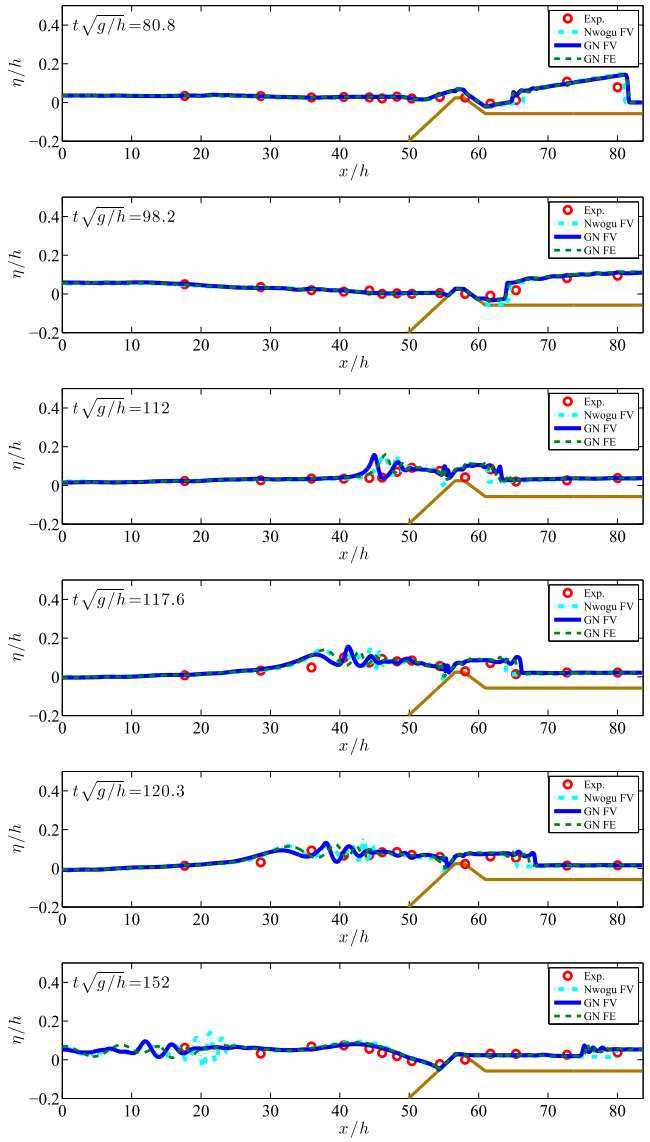

Fig. 25. Evolution of surface profiles and wave transformations over an exposed reef for $A/h = 0.3$ and $1/12$ slope.

lag in the results between two formulations is revealed in the region after breaking, perhaps related to the perturbation disturbing the upstream signal. The results produced by the second formulation are closer to the experimental data.

In conclusion we can say that even though the first formulation has the advantage that the elliptic and hyperbolic parts are completely independent and easy to implement in any formulation, it seems more oscillatory than the second approach which switches-off the dispersion terms in a more smooth way. Of course further research on the topic is in need, which will involve the usage of different discretization schemes and irregular meshes.

8. Conclusions

In this paper, we propose and study a flexible and unsplit strategy to enhance a shallow water code to embed the fully-nonlinear weakly dispersive effects of the Green–Naghdi equations [41,42]. The main contributions of the paper may be summarized as follows:

- We have proposed a decoupled unsplit formulation which allows to enhance a (hyperbolic) shallow water code by a purely algebraic correction to the discrete momentum equation. This correction can be computed from the solution of a stationary elliptic problem to embed both the fully-nonlinear weakly dispersive effects, and wave breaking;

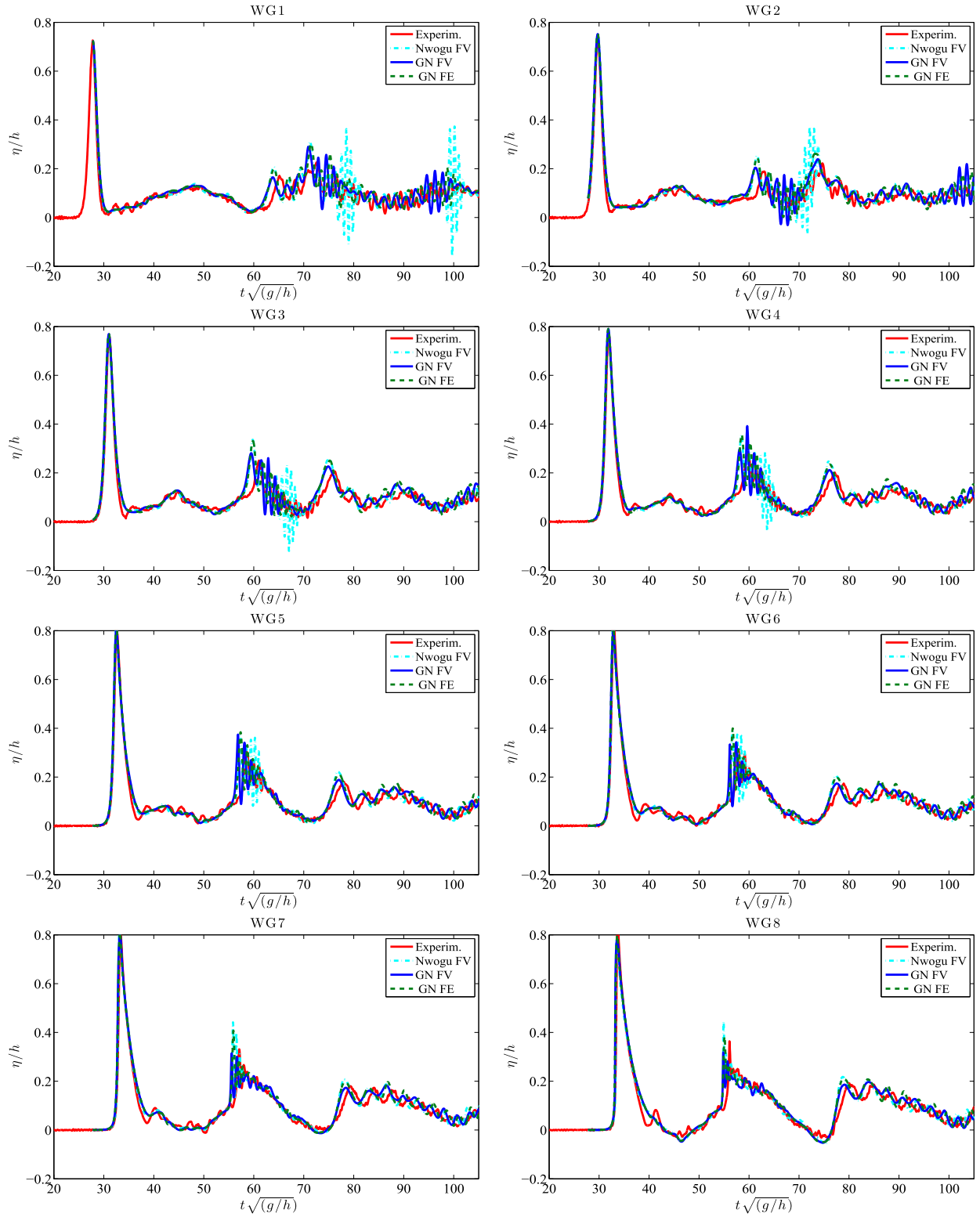

Fig. 26. Time series of the normalized free surface at the wave gauges before the reef.

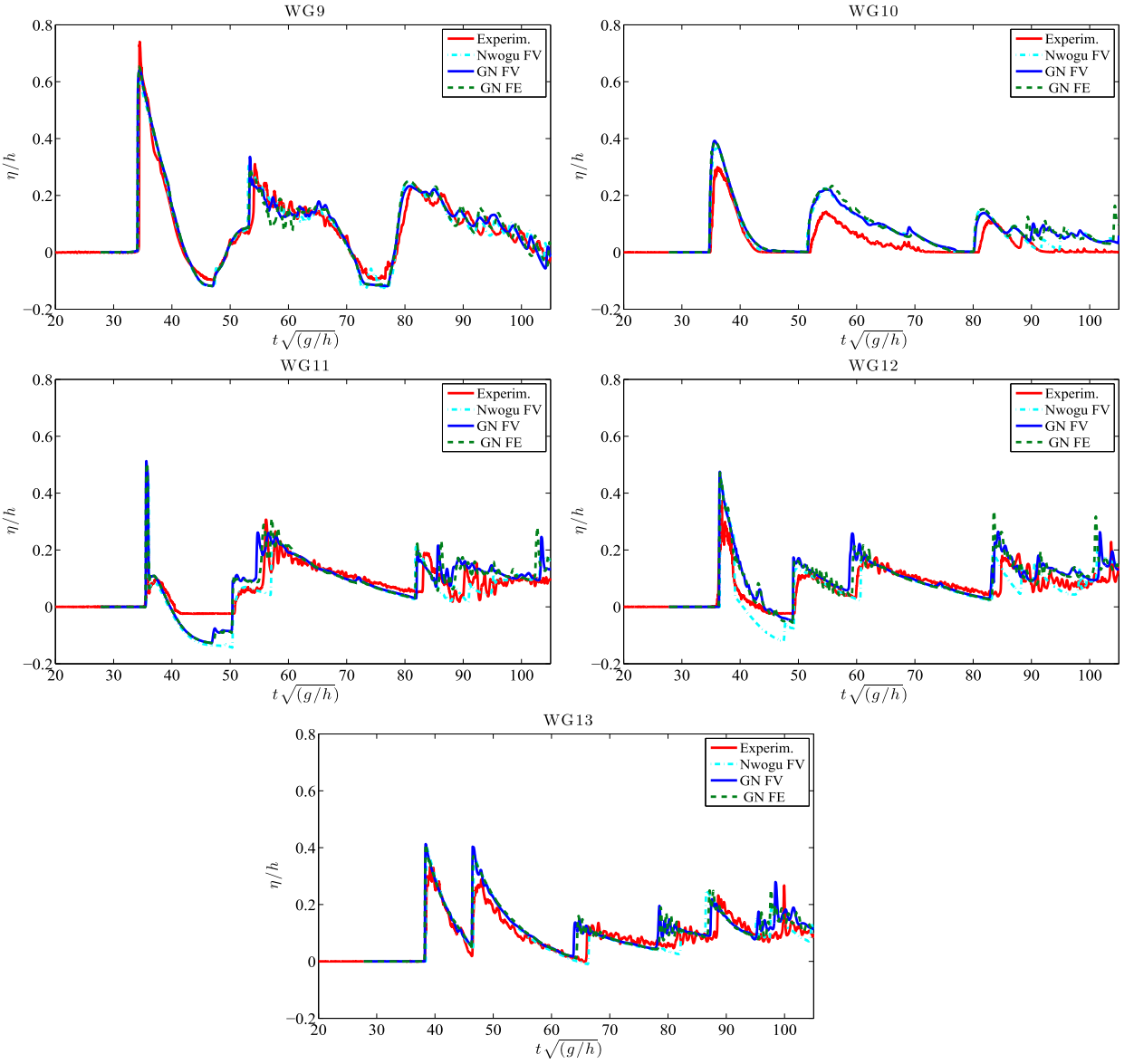

Fig. 27. Time series of the normalized free surface at the wave gauges on top and after the reef.

- To evaluate the potential of this enhancement technique, we have investigated hybrid discretizations in which different methods are used in the two different phases (elliptic solver, hyperbolic evolution step). Several methods are thus tested both in space and in time, involving both finite element and finite volume methods in space, and both multi-stage and multi-step methods in time. In particular, we have focused on the use of a C^0 Galerkin approximation of the variational form of the elliptic problem, and on the use of both upwind finite volumes [53,37], Galerkin and stabilized Galerkin finite elements [60,6,7];
- Time continuous dispersion analysis. This analysis has shown several important facts. First, the behavior obtained when coupling the continuous Galerkin elliptic solver with different hyperbolic methods is quite similar. This confirms the flexibility of our approach. Second, an essential role is played by the approximation of the third order derivatives in the right hand side of the elliptic solver. Exact integration to evaluate this term allows to recover, for all the combinations considered, dispersion errors of the same order, or smaller, than those provided by fourth order finite differencing. Lastly, we find that the use of a properly designed second order accurate discretization for the elliptic phase is enough to achieve such low levels of dispersion errors, provided that at least third order of accuracy is guaranteed for the hyperbolic component. This is true for all the different combinations of the elliptic–hyperbolic methods considered. This result generalizes previous findings and constructions in the finite difference context (see e.g. Wei et al. [79]). Our

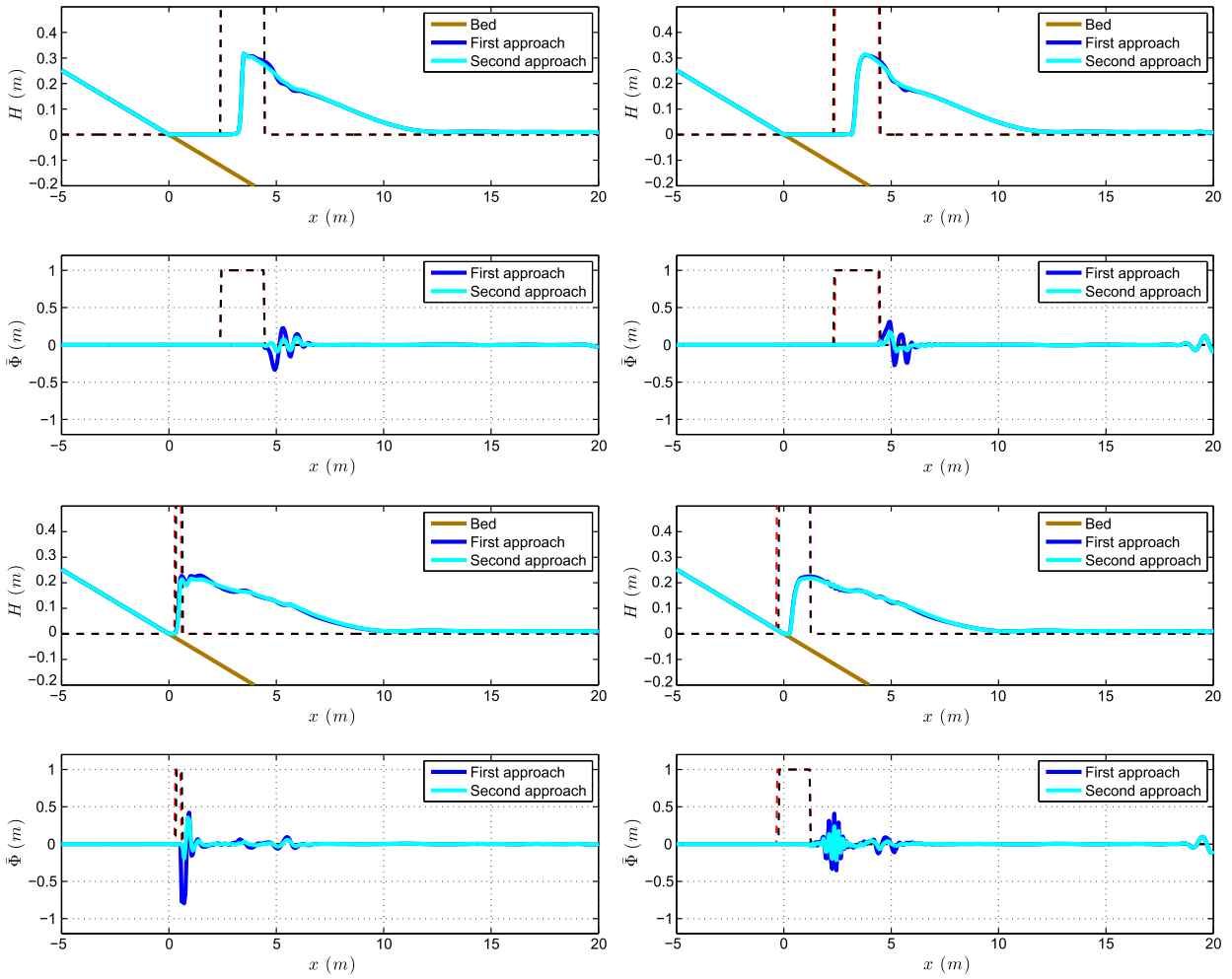

Fig. 28. Surface elevation and $\bar{\Phi}$ for FV and SUPG scheme for a solitary wave of $\epsilon = 0.28$.

analysis show that this approach allows enough flexibility to enhance many of the existing shallow water codes based on finite element and finite volume discretizations;

- Dispersion analysis of the time discretization. The analysis of the time discretization of the unsplit linearized operator has been performed. We have shown the equivalence of this operator with a modified form of the linearized shallow water system with a celerity dependent on the wavenumber. The analysis has allowed to compare the dispersion errors of three different discretizations: the standard SSP Runge–Kutta 3 method [30], the third order extrapolated backward difference method [34], and the predictor corrector Adams–Bashforth/Adams–Moulton predictor corrector method [79, 62]. All these approaches have been found to provide a fourth order approximation of the phase. However, the RK3 and eBDf3 methods have shown a slope three for the amplification rate, thus confirming third order of accuracy. For the AM method, we find a fifth order rate of convergence for the amplification rate, thus confirming the fourth order of accuracy of the scheme. The choice between the three methods can thus be made in terms of other considerations (e.g. SSP property for RK3, effective CFL for the AM method, easy generalization to higher orders, etc.).
- We have studied the effects of embedding the breaking mask in the elliptic phase, in the hope of reducing spurious oscillations arising form the coupling of Green–Naghdi and shallow water in breaking regions, as proposed by many in the past [75,72,36,37]. The approach is shown to reduce considerably spurious oscillations in the proximities of the breaking region. However, it does not resolve issues related to the intermittency of the breaking detection and, unfortunately, still leaves open the problem of obtaining fully mesh converged solutions for the coupled model;
- We have validated the approach proposed, using all the combinations of the schemes tested, on smooth and non-smooth flows, involving wave braking and overtopping. Our results compare very favorably with analytical solutions, showing an order of convergence in between 2.5 and 3, and with experimental data. Computations on perturbed meshes also show very little sensitivity, proving the potential of this approach for applications on fully unstructured meshes.

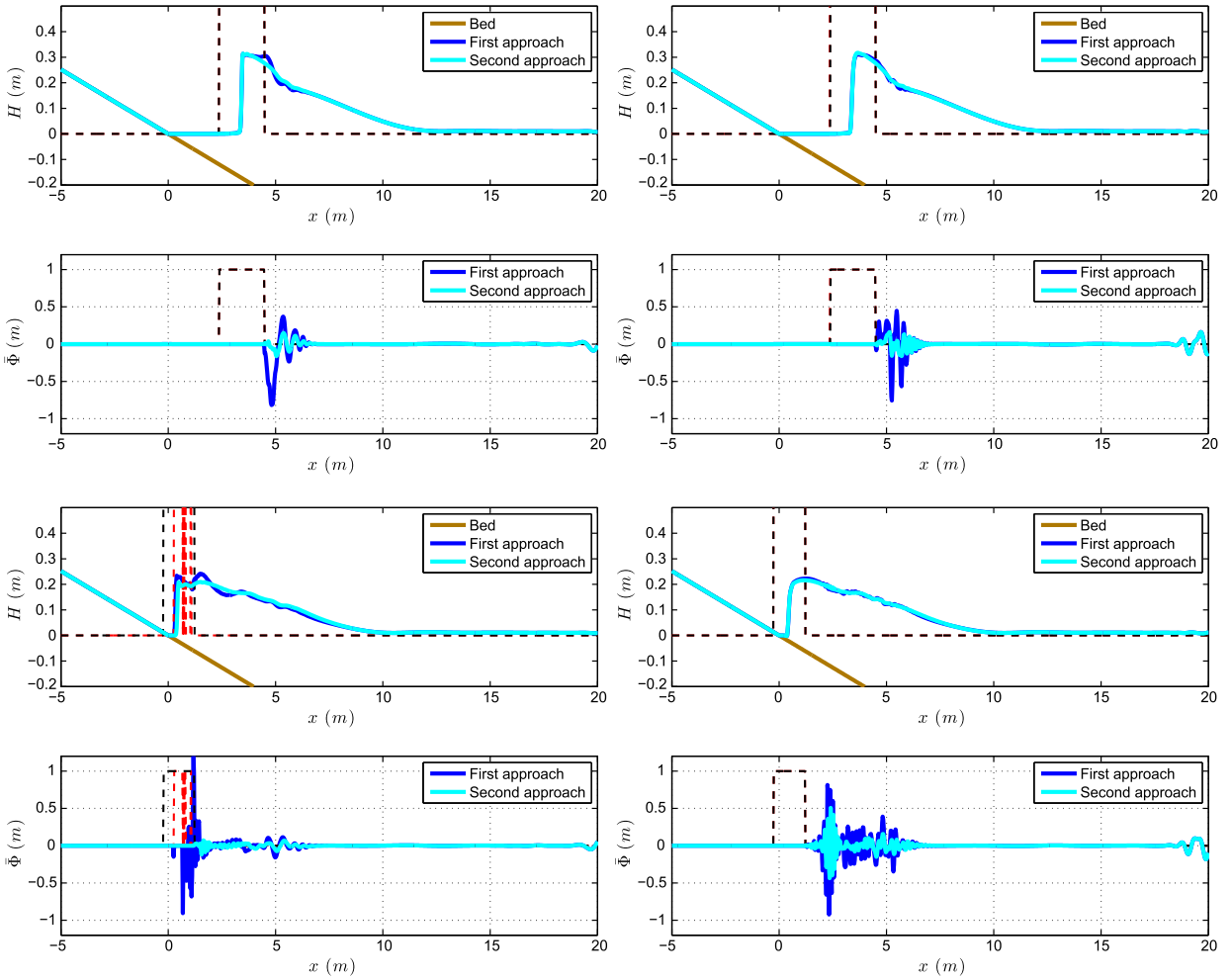

Fig. 29. Surface elevation and $\bar{\Phi}$ for FV and SUPG scheme for a solitary wave of $\epsilon = 0.28$ and a refined mesh.

We consider that our results show that the approach proposed has enormous potential as a non-intrusive enhancement technique for existing shallow water solvers.

The work done highlights several issues still open and provides many research avenues. Of course the first urgent issue is the generalization and exploitation of this approach in the multidimensional case on adaptive unstructured meshes. This is already ongoing work.

Another interesting issue is the comparison of the gains in dispersion accuracy when enhancing the elliptic solver from second to higher order, and w.r.t. the number of points per wavelength. This study should allow to estimate the trade-off between the cost of inverting a stiffer (and possibly larger) algebraic system and the reduction in number of points/wavelength, potentially obtained with this enhancement.

Perhaps the most critical problem is the well-posedness of the coupling dispersive-hydrostatic in the breaking region. Despite all of our efforts with the current model, and with similar past implementations [36,37,6,7], we have never been able to obtain a fully mesh converged result with this modelling method. We think that the well-posedness of this procedure may be questionable and that this should be investigated in the future. We stress that this behavior may hinder the use of efficient local adaptation techniques to capture breaking fronts more accurately. Alternative approaches to model wave breaking, based on the use of turbulence models to improve dissipation, based on an eddy viscosity [55,26,14], are also being explored.

Other future directions involve the coupling of continuous finite elements for the elliptic phase with discontinuous Galerkin methods for the hyperbolic one, possibly with a lower order continuous approximation for the elliptic phase to further reduce the algebraic costs, and the use of dynamic unstructured mesh adaptation techniques as those proposed e.g. in [1] or in [18,4,5].

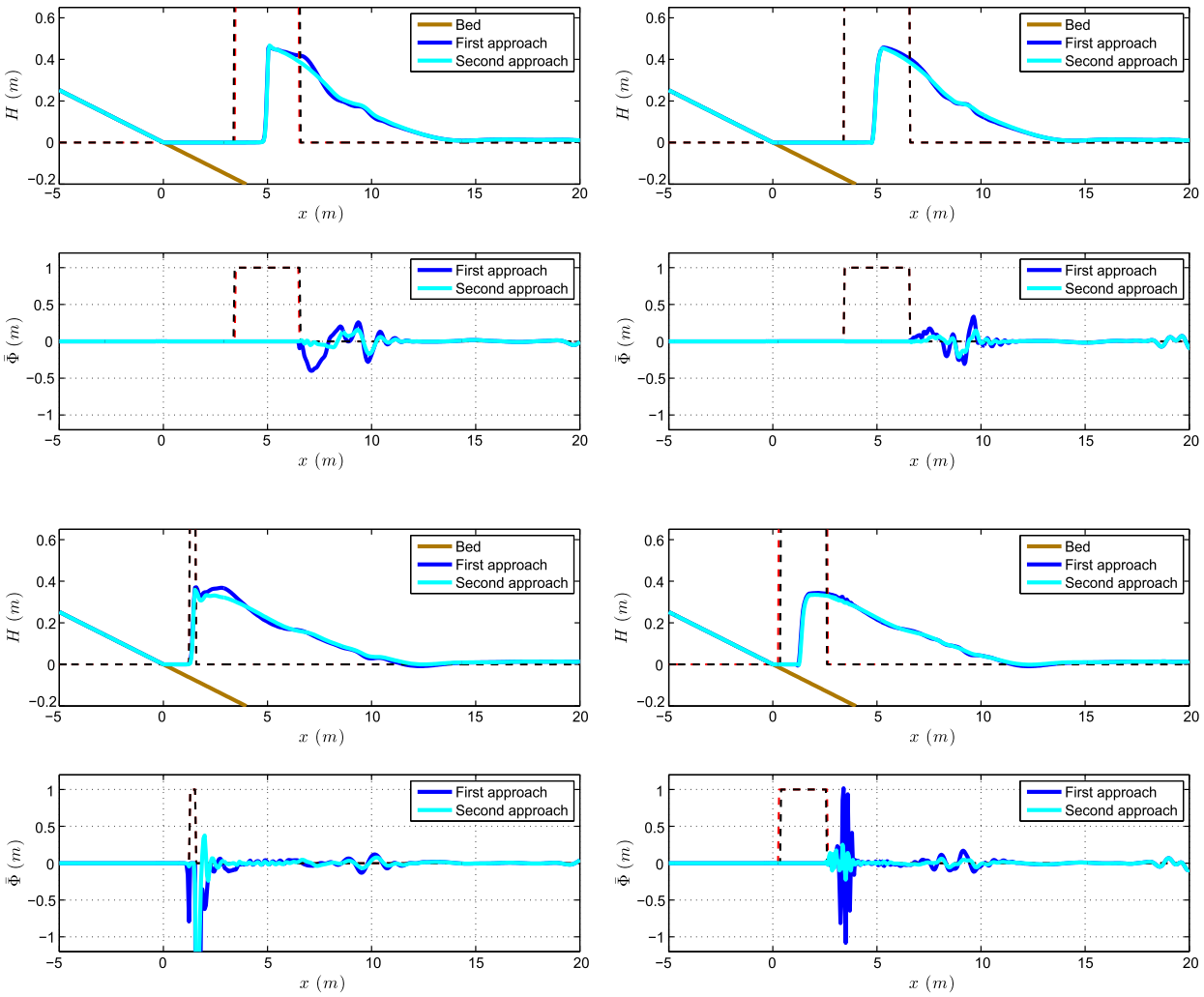

Fig. 30. Surface elevation and $\tilde{\Phi}$ for FV and SUPG scheme for a solitary wave of $\epsilon = 0.5$.

Acknowledgements

Work partially funded by the TANDEM contract, reference ANR-11-RSNR-0023-01 of the French *Programme Investissements d'Avenir*.

Appendix A

We report here the definitions of the several quantities called in section 5 and involved in the analysis of the dispersion properties of the schemes. Moreover, the paragraph contains the expressions of the dispersion relation formulae of the FD2 and FD4 schemes used as comparison in figures from 2 to 5 and the description of the several configurations (from 1 to 4) taken into account for the elliptic problem discretization.

The quantities involved in the dispersion analysis, see for example system (49), are easily computed from the finite difference form of the scheme, and read:

- the Galerkin mass matrix: $\tilde{\mathrm{M}}^{\mathrm{G}} = \frac{1}{6}\left(4 + 2\cos\bar{\mu}\right)$;
- the solution of the elliptic problem: $\tilde{\Phi}_{LIN} = -\frac{gh_0^3}{3}\tilde{\mathrm{T}}^{\mathrm{G}}\left(\tilde{\mathrm{M}}^{\mathrm{G}}\right)^{-1}\left(\tilde{\mathrm{M}}^{\mathrm{G}} - \frac{\alpha h_0^2}{3}\tilde{\mathrm{S}}^{\mathrm{G}}\right)^{-1}$

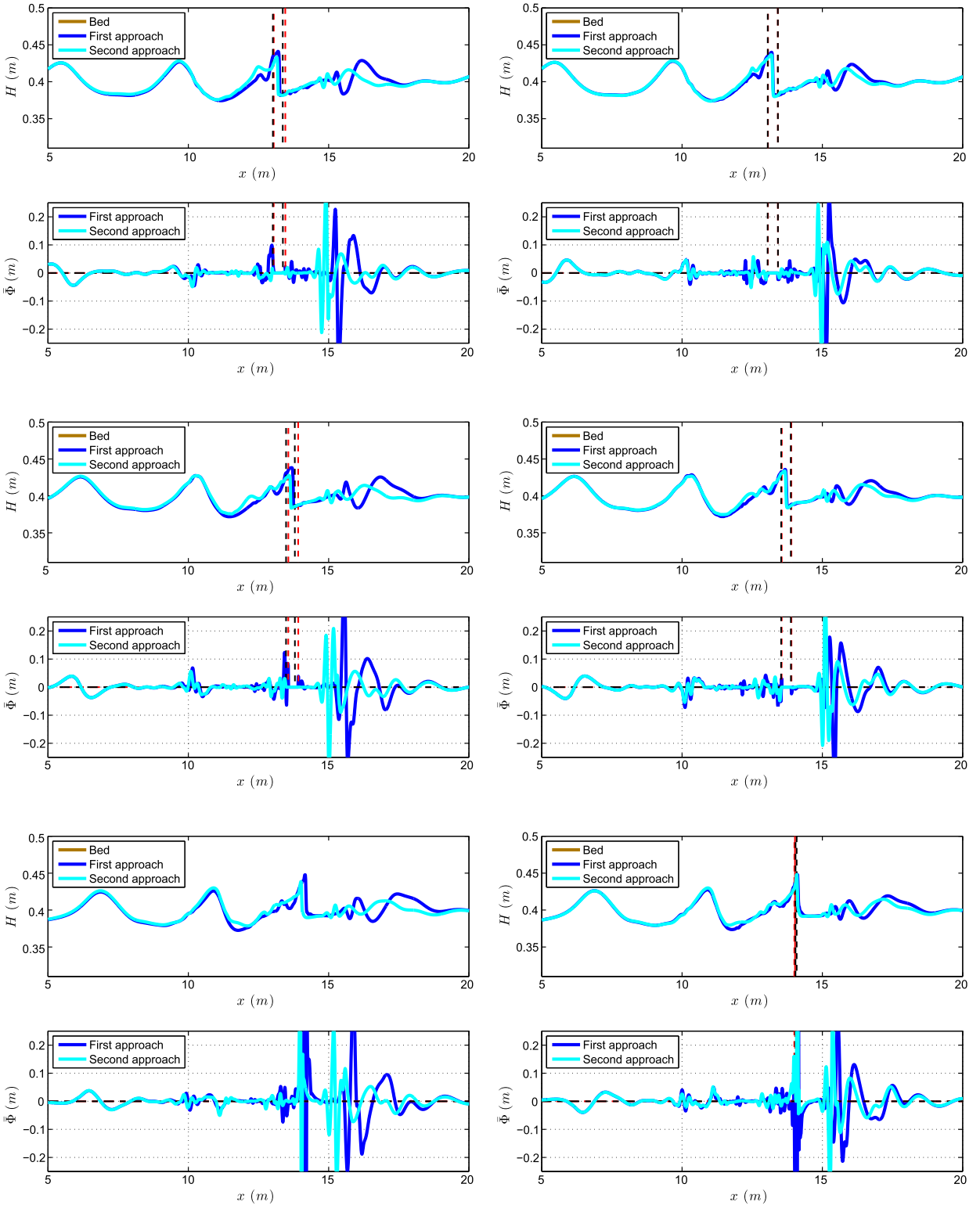

Fig. 31. Surface elevation and $\bar{\Phi}$ for FV and SUPG scheme for a solitary wave over a bar.

and the Galerkin discretization of:

- the first order space derivatives $\partial_x(\cdot)$: $\tilde{\mathrm{F}}^{\mathrm{G}} = j\frac{k}{2\bar{\mu}}\left(2\sin\bar{\mu}\right)$;
- the second order space derivatives $\partial_{xx}(\cdot)$: $\tilde{\mathrm{S}}^{\mathrm{G}} = \frac{k^2}{\bar{\mu}^2}\left(2\cos\bar{\mu} - 2\right)$;
- the third order space derivatives $\partial_{xxx}(\cdot)$: $\tilde{\mathrm{T}}^{\mathrm{G}} = j\frac{k^3}{2\bar{\mu}^3}\left(2\sin 2\bar{\mu} - 4\sin\bar{\mu}\right)$;

where $\bar{\mu} = k\Delta x$ and k represents the wavenumber associated to the Fourier mode.

For the Galerkin scheme, the phase resulting from the condition that the matrix of system (49) has zero determinant is

$$\left(\omega_{\Delta x}^{\mathrm{G}}\right)^2 = \frac{gh_0\left(\tilde{\mathrm{F}}^{\mathrm{G}}\right)^2 - \tilde{\mathrm{F}}^{\mathrm{G}}\tilde{\mathrm{M}}^{\mathrm{G}}\tilde{\Phi}_{LIN}}{\left(\tilde{\mathrm{M}}^{\mathrm{G}}\right)^2} \tag{A.1}$$

The amplification rate is found to be identically equal to zero (no dumping or amplification).

The analysis is more complex for the SUPG scheme. Being $c = gh_0$ the celerity of the wave, the sign of the Jacobian matrix of the linear shallow water fluxes, which pre-multiplies the upwind terms in (31), has the form:

$$\mathrm{sign}(A) = \begin{bmatrix} 0 & c/g \\ g/c & 0 \end{bmatrix}.$$

Discretizing system (46) by means of the SUPG scheme will now lead to:

$$\left(\tilde{\mathrm{M}}^{\mathrm{G}} - \frac{\alpha h_0^2}{3}\tilde{\mathrm{S}}^{\mathrm{G}}\right)\phi_i = -\frac{gh_0^3}{3}\tilde{\mathrm{T}}^{\mathrm{G}}\left(\tilde{\mathrm{M}}^{\mathrm{G}}\right)^{-1}\eta_i \tag{A.2}$$

$$\tilde{\mathrm{M}}^{\mathrm{G}}\nu_{\Delta x}\eta_i + h_0\tilde{\mathrm{F}}^{\mathrm{G}}u_i - \frac{c}{2g}\left[\tilde{\mathrm{M}}^{\mathrm{UFE}}\nu_{\Delta x}u_i + g\tilde{\mathrm{F}}^{\mathrm{UFE}}\eta_i - \frac{1}{h_0}\tilde{\mathrm{M}}^{\mathrm{UFE}}\phi_i\right] = 0 \tag{A.3}$$

$$\tilde{\mathrm{M}}^{\mathrm{G}}\nu_{\Delta x}u_i + g\tilde{\mathrm{F}}^{\mathrm{G}}\eta_i - \frac{g}{2c}\left[\tilde{\mathrm{M}}^{\mathrm{UFE}}\nu_{\Delta x}\eta_i + h_0\tilde{\mathrm{F}}^{\mathrm{UFE}}u_i\right] = \frac{1}{h_0}\tilde{\mathrm{M}}^{\mathrm{G}}\phi_i$$

the two quantities $\tilde{\mathrm{M}}^{\mathrm{UPE}}$ and $\tilde{\mathrm{F}}^{\mathrm{UPE}}$ derive from the FE discretization of the upwind flux and have the following form:

- $\tilde{\mathrm{M}}^{\mathrm{UFE}} = j\sin\bar{\mu}$
- $\tilde{\mathrm{F}}^{\mathrm{UFE}} = \frac{k}{\bar{\mu}}\left(2\cos\bar{\mu} - 2\right)$

The writing of the Jacobian matrix of the system (A.3) and of its characteristic polynomial lead to a complex algebraic equation, whose solution in the real part can be written in the form:

$$\left(\omega_{\Delta x}^{\mathrm{SU}}\right)^2 = \frac{\mathrm{A}_S^{\mathrm{SU}}}{\mathrm{A}_{\nu^2}^{\mathrm{SU}}} - \left(\frac{\mathrm{A}_\nu^{\mathrm{SU}}}{2\mathrm{A}_{\nu^2}^{\mathrm{SU}}}\right)^2 \tag{A.4}$$

where $\mathrm{A}_{\nu^2}^{\mathrm{SU}}$, $\mathrm{A}_\nu^{\mathrm{SU}}$ and $\mathrm{A}_S^{\mathrm{SU}}$ are functions of the just defined quantities $\tilde{\mathrm{M}}^{\mathrm{G}}$, $\tilde{\mathrm{F}}^{\mathrm{G}}$, $\tilde{\mathrm{M}}^{\mathrm{UPE}}$, $\tilde{\mathrm{F}}^{\mathrm{UPE}}$ and $\tilde{\Phi}_{LIN}$.

Concerning the FV scheme, using the linearized equations (47) and the third order MUSCL reconstruction, described in section 3.3, we get for the following system of equations:

$$\left(\tilde{\mathrm{M}}^{\mathrm{G}} - \frac{\alpha h_0^2}{3}\tilde{\mathrm{S}}^{\mathrm{G}}\right)\phi_i = -\frac{gh_0^3}{3}\tilde{\mathrm{T}}^{\mathrm{G}}\left(\tilde{\mathrm{M}}^{\mathrm{G}}\right)^{-1}\eta_i \tag{A.5}$$

$$\nu_{\Delta x}\eta_i + h_0\tilde{\mathrm{F}}^{\mathrm{FV}}u_i - c\tilde{\mathrm{F}}^{\mathrm{UFV}}\eta_i = 0 \tag{A.6}$$

$$\nu_{\Delta x}u_i + g\tilde{\mathrm{F}}^{\mathrm{FV}}\eta_i - c\tilde{\mathrm{F}}^{\mathrm{UFV}}u_i = \frac{1}{h_0}\tilde{\mathrm{M}}^{\mathrm{FV}}\phi_i$$

which, by means of the procedure already described above for the SUPG scheme, lead to the final form of the dispersion relation:

$$\left(\omega_{\Delta x}^{\mathrm{FV}}\right)^2 = \frac{\mathrm{A}_S^{\mathrm{FV}}}{\mathrm{A}_{\nu^2}^{\mathrm{FV}}} - \left(\frac{\mathrm{A}_\nu^{\mathrm{FV}}}{2\mathrm{A}_{\nu^2}^{\mathrm{FV}}}\right)^2 \tag{A.7}$$

being $A^{FV}_{\nu^2}$, A^{FV}_{ν} and A^{FV}_{S} functions of the quantities $\tilde{M}^{FV}$, $\tilde{F}^{FV}$, $\tilde{F}^{UFV}$ and $\tilde{\Phi}_{LIN}$, whose expressions comes from the discretization of the:

- elliptic term $\overline{\Phi}$: $\tilde{M}^{FV} = \frac{1}{6}\left(6 + 2\cos\bar{\mu}\right)$
- centered fluxes: $\tilde{F}^{FV} = j\frac{k}{2\bar{\mu}}\left(\frac{8}{3}\sin\bar{\mu} - \frac{1}{3}\sin 2\bar{\mu}\right)$
- upwind fluxes: $\tilde{F}^{UFV} = \frac{k}{2\bar{\mu}}\left(\frac{4}{3}\cos\bar{\mu} - \frac{1}{3}\cos 2\bar{\mu} - 1\right)$

Figures from 2 to 5 show the dispersion errors of the several schemes w.r.t. the analytical dispersion relation of the model given by (7). The comparison is made for low and high values of the parameter kh_0 w.r.t. the errors provided by the FD2 and FD4 discretization schemes, whose dispersion relations are respectively:

$$\left(\omega^{FD2}_{\Delta x}\right)^2 = gh_0\left(\tilde{F}^{FD2}\right)^2 - \tilde{F}^{FD2}\tilde{\Phi}^{(FD2)}_{LIN} \tag{A.8}$$

$$\left(\omega^{FD4}_{\Delta x}\right)^2 = gh_0\left(\tilde{F}^{FD4}\right)^2 - \tilde{F}^{FD4}\tilde{\Phi}^{(FD4)}_{LIN} \tag{A.9}$$

where the introduced tensors are defined in the following and come from the second order finite difference:

- discretization of the first order space derivatives $\partial_x(\cdot)$: $\tilde{F}^{FD2} = \tilde{F}^{G}$
- discretization of the second order space derivatives $\partial_{xx}(\cdot)$: $\tilde{S}^{FD2} = \tilde{F}^{G}$
- discretization of the first order space derivatives $\partial_{xxx}(\cdot)$: $\tilde{T}^{FD2} = \tilde{F}^{G}$
- solution of the elliptic problem: $\tilde{\Phi}^{(FD2)}_{LIN} = -\frac{gh_0^3}{3}\tilde{T}^{FD2}\left(1 - \frac{\alpha h_0^2}{3}\tilde{S}^{FD2}\right)^{-1}$

and from the fourth order finite difference:

- discretization of the first order space derivatives $\partial_x(\cdot)$: $\tilde{F}^{FD4} = j\frac{k}{12\bar{\mu}}\left(-2\sin 2\bar{\mu} + 16\sin\bar{\mu}\right)$
- discretization of the second order space derivatives $\partial_{xx}(\cdot)$: $\tilde{S}^{FD4} = \frac{k^2}{12\bar{\mu}^2}\left(-2\cos 2\bar{\mu} + 32\cos\bar{\mu} - 30\right)$
- discretization of the first order space derivatives $\partial_{xxx}(\cdot)$: $\tilde{T}^{FD4} = j\frac{k^3}{8\bar{\mu}^3}\left(-2\sin 3\bar{\mu} + 16\sin 2\bar{\mu} - 26\sin\bar{\mu}\right)$
- solution of the elliptic problem: $\tilde{\Phi}^{(FD4)}_{LIN} = -\frac{gh_0^3}{3}\tilde{T}^{FD4}\left(1 - \frac{\alpha h_0^2}{3}\tilde{S}^{FD4}\right)^{-1}$

Finally, we give in the following the descriptions of the four different configurations studied for the discretization of the elliptic equation (48), whose dispersion errors are compared each other in Figs. 3, 4 and 5.

1) it stands for the choice to lump both the mass matrices of the equations (11) and (17). Equation (48) thus becomes $\left(1 - \frac{\alpha h_0^2}{3}\tilde{S}^{G}\right)\phi_i = -\frac{gh_0^3}{3}\tilde{T}^{G}\eta_i$ and the related $\tilde{\Phi}_{LIN}$ takes the form:

$$\tilde{\Phi}^{(1)}_{LIN} = -\frac{gh_0^3}{3}\tilde{T}^{G}\left(1 - \frac{\alpha h_0^2}{3}\tilde{S}^{G}\right)^{-1}$$

2) it stands for the choice to lump only the mass matrix of equation (17). Equation (48) thus becomes $\left(\tilde{M}^{G} - \frac{\alpha h_0^2}{3}\tilde{S}^{G}\right)\phi_i = -\frac{gh_0^3}{3}\tilde{T}^{G}\eta_i$ and the related $\tilde{\Phi}_{LIN}$ takes the form:

$$\tilde{\Phi}^{(2)}_{LIN} = -\frac{gh_0^3}{3}\tilde{T}^{G}\left(\tilde{M}^{G} - \frac{\alpha h_0^2}{3}\tilde{S}^{G}\right)^{-1}$$

3) it stands for the choice to lump only the mass matrix of equation (11). Equation (48) thus becomes $\left(1 - \frac{\alpha h_0^2}{3}\tilde{S}^{G}\right)\phi_i = -\frac{gh_0^3}{3}\tilde{T}^{G}\left(\tilde{M}^{G}\right)^{-1}\eta_i$ and the related $\tilde{\Phi}_{LIN}$ takes the form:

$$\tilde{\Phi}^{(3)}_{LIN} = -\frac{gh_0^3}{3}\tilde{T}^{G}\left(\tilde{M}^{G}\right)^{-1}\left(1 - \frac{\alpha h_0^2}{3}\tilde{S}^{G}\right)^{-1}$$

4) it stands for the choice not to lump any mass matrix. Equation (48) thus don't change and the related $\tilde{\Phi}_{LIN}$ is given by:

$$\tilde{\Phi}^{(4)}_{LIN} = -\frac{gh_0^3}{3}\tilde{T}^G\left(\tilde{M}^G\right)^{-1}\left(\tilde{M}^G - \frac{\alpha h_0^2}{3}\tilde{S}^G\right)^{-1}$$

References

[1] F. Alauzet, P.J. Frey, P.L. George, B. Mohammadi, 3d transient fixed point mesh adaptation for time-dependent problems: application to CFD simulations, J. Comput. Phys. 222 (2) (March 2007) 592–623.
[2] B. Alvarez-Samaniego, D. Lannes, A Nash–Moser theorem for singular evolution equations. Application to the Serre and Green–Naghdi equations, Indiana Univ. Math. J. 57 (1) (2008).
[3] J.S. Antunes do Carmo, F.J. Seabra-Santos, A.B. Almeida, Numerical solution of the generalized Serre equations with the MacCormack finite-difference scheme, Int. J. Numer. Methods Fluids 16 (1993) 725–738.
[4] L. Arpaia, M. Ricchiuto, Well-balanced ALE: a framework for time dependent mesh adaptation for the shallow water equations, in: SIAM Conference on Nonlinear Waves and Coherent Structures, Cambridge, United Kingdom, August 2014.
[5] L. Arpaia, M. Ricchiuto, Mesh adaptation by continuous deformation. Basics: accuracy, efficiency, well balancedness, Research report RR-8666, Inria Bordeaux Sud-Ouest, INRIA, January 2015.
[6] P. Bacigaluppi, M. Ricchiuto, P. Bonneton, A 1d stabilized finite element model for non-hydrostatic wave breaking and run-up, in: J. Fuhrmann, M. Ohlberger, C. Rohde (Eds.), Finite Volumes for Complex Applications VII, in: Springer Proc. Math. Stat., vol. 77, Springer, 2014.
[7] P. Bacigaluppi, M. Ricchiuto, P. Bonneton, Upwind stabilized finite element modelling of non-hydrostatic wave breaking and run-up, Research report RR-8536, May 2014.
[8] S. Beji, J.A. Battjes, Experimental investigations of wave propagation over a bar, Coast. Eng. 19 (1993) 151.
[9] A. Bermudez, M.E. Vazquez, Upwind methods for hyperbolic conservation laws with source terms, Comput. Fluids 23 (8) (1994) 1049–1071.
[10] H.B. Bingham, P.A. Madsen, D.R. Fuhraman, Velocity potential formulations of highly accurate Boussinesq-type models, Coast. Eng. 56 (2009) 467.
[11] P. Bonneton, E. Barthelemy, F. Chazel, R. Cienfuegos, D. Lannes, F. Marche, M. Tissier, Recent advances in Serre–Green Naghdi modelling for wave transformation, breaking and runup processes, Eur. J. Mech. B Fluids 30 (2011) 589–597.
[12] P. Bonneton, F. Chazel, D. Lannes, F. Marche, M. Tissier, A splitting approach for the fully nonlinear and weakly dispersive Green–Naghdi model, J. Comput. Phys. 230 (2011) 1479–1498.
[13] A.G.L. Borthwick, M. Ford, B.P. Weston, P.H. Taylor, P.K. Stansby, Solitary wave transformation, breaking and run-up at a beach, Marit. Eng. 159 (2006) 97–105.
[14] R. Briganti, R. Musumeci, R.E. Belloti, M. Brocchini, E. Foti, Boussinesq modeling of breaking waves: description of turbulence, J. Geophys. Res. 109 (2004).
[15] M. Brocchini, A reasoned overview on Boussinesq-type models: the interplay between physics, mathematics and numerics, Proc. R. Soc. A 469 (2013) 20130496.
[16] P. Brufau, P. García-Navarro, M.E. Vázquez-Cendón, Zero mass error using unsteady wetting-drying conditions in shallow flows over dry irregular topography, Int. J. Numer. Methods Fluids 45 (2004) 1047–1082.
[17] P. Brufau, M.E. Vázquez-Cendón, P. Gracía-Navarro, A numerical model for the flooding and drying of irregular domains, Int. J. Numer. Methods Fluids 39 (2002) 247–275.
[18] C.J. Budd, W. Huang, R.D. Russell, Adaptivity with moving grids, Acta Numer. 18 (2009) 111–241.
[19] M.J. Castro, A.M. Ferreiro, J.A. García-Rodriguez, J.M. González-Vida, J. Macías, C. Parés, M.E. Vázquez-Cendón, The numerical treatment of wet/dry fronts in shallow flows: application to one-layer and two-layer systems, Math. Comput. Model. 42 (2005) 419–439.
[20] F. Chazel, D. Lannes, F. Marche, Numerical simulation of strongly nonlinear and dispersive waves using a Green–Naghdi model, J. Sci. Comput. 48 (2011) 105–116.
[21] A. Chertock, S. Cui, A. Kurganov, T. Wu, Steady state and sign preserving semi-implicit Runge–Kutta methods for ODEs with stiff damping term, SIAM J. Numer. Anal. 53 (2015) 2008–2029.
[22] R. Cienfuegos, E. Barthélemy, P. Bonneton, A fourth-order compact finite volume scheme for fully nonlinear and weakly dispersive Boussinesq-type equations. Part I: model development and analysis, Int. J. Numer. Methods Fluids 51 (2006) 1217–1253.
[23] R. Cienfuegos, E. Barthélemy, P. Bonneton, A fourth-order compact finite volume scheme for fully nonlinear and weakly dispersive Boussinesq-type equations. Part II: boundary conditions and validation, Int. J. Numer. Methods Fluids 53 (2007) 1423–1455.
[24] R. Cienfuegos, E. Barthélemy, P. Bonneton, Wave-breaking model for Boussinesq-type equations including roller effects in the mass conservation equation, J. Waterw. Port Coast. Ocean Eng. 136 (2010) 10–26.
[25] A.I. Delis, I.K. Nikolos, M. Kazolea, Performance and comparison of cell-centered and node-centered unstructured finite volume discretizations for shallow water free surface flows, Arch. Comput. Methods Eng. 18 (2011) 57–118.
[26] Z. Demirbilek, A. Zundel, O. Nwogu, Boussinesq modeling of wave propagation and runup over fringing coral reefs, model evaluation report, Coastal and Hydraulics Laboratory Technical Note CHLTR0712, U.S. Army Engineer Research and Development Center, Vicksburg, MS, 2007.
[27] A. Duran, F. Marche, Discontinuous-Galerkin discretization of a new class of Green–Naghdi equations, Commun. Comput. Phys. (2014) 130.
[28] K.S. Erduran, S. Ilic, V. Kutija, Hybrid finite-volume finite-difference scheme for the solution of Boussinesq equations, Int. J. Numer. Methods Fluids 49 (2005) 1213–1232.
[29] A.G. Filippini, S. Bellec, M. Colin, M. Ricchiuto, On the nonlinear behavior of Boussinesq type models: amplitude-velocity vs amplitude-flux forms, Coast. Eng. (2015), http://dx.doi.org/10.1016/j.coastaleng.2015.02.003.
[30] S. Gottlieb, C.-W. Shu, E. Tadmor, Strong stability-preserving high-order time discretization methods, SIAM Rev. (1) (2001) 89–112.
[31] A.E. Green, P.M. Naghdi, A derivation of equations for wave propagation in water of variable depth, J. Fluid Mech. 78 (1976) 237–246.
[32] M.E. Hubbard, P. García-Navarro, Flux difference splitting and the balancing of source terms and flux gradients, J. Comput. Phys. 165 (2000) 89–125.
[33] T.J.R. Hughes, G. Scovazzi, T. Tezduyar, Stabilized methods for compressible flows, J. Sci. Comput. 43 (2010) 343–368.
[34] W. Hundsdorfer, S.J. Ruuth, R.J. Spiteri, Monotonicity-preserving linear multistep methods, SIAM J. Numer. Anal. 41 (2003) 605–623.
[35] W. Hundsdorfer, J.G. Verwer, Numerical Solution of Time-Dependent Advection-Diffusion-Reaction Equations, Springer Series in Comput. Math., Springer, 2003.
[36] M. Kazolea, A.I. Delis, A well-balanced shock-capturing hybrid finite volume-finite difference numerical scheme for extended 1D Boussinesq models, Appl. Numer. Math. 67 (2013) 167–186.
[37] M. Kazolea, A.I. Delis, C.E. Synolakis, Numerical treatment of wave breaking on unstructured finite volume approximations for extended Boussinesq-type equations, J. Comput. Phys. 271 (2014) 281–305.
[38] M.J. Kermani, A.G. Geber, J.M. Stockie, Thermodynamically based moisture prediction using Roe's scheme, in: The 4th Conference of Iranian AeroSpace Society, Amir Kabir University of Technology, Tehran, Iran, January 2003.

[39] J. Klosa, Extrapolated BDF residual distribution schemes for the shallow water equations, Master thesis, 2012.
[40] D. Lannes, The Water Waves Problem: Mathematical Analysis and Asymptotics, American Mathematical Society, Providence, Rhode Island, 2013.
[41] D. Lannes, P. Bonneton, Derivation of asymptotic two-dimensional time-dependent equations for surface water wave propagation, Phys. Fluids 21 (2009).
[42] D. Lannes, F. Marche, A new class of fully nonlinear and weakly dispersive Green–Naghdi models for efficient 2d simulations, J. Comput. Phys. 282 (2015) 238–268.
[43] R.J. LeVeque, Finite Volume Methods for Hyperbolic Problems, Cambridge University Press, 2002.
[44] M. Li, P. Guyenne, F. Li, L. Xu, High-order well-balanced CDG-FE methods for shallow water waves by a Green–Naghdi model, J. Comput. Phys. 257 (2014) 169–192.
[45] Q. Liang, A.G.L. Borthwick, Adaptive quadtree simulation of shallow flows with wet/dry front over complex topography, Comput. Fluids 38 (2009) 221–234.
[46] P.J. Lynett, Nearshore wave modeling with high-order Boussinesq-type equations, J. Waterw. Port Coast. Ocean Eng. 132 (2006) 348–357.
[47] P.A. Madsen, H.A. Schäffer, Higher-order Boussinesq-type equations for surface gravity waves: derivation and analysis, Philos. Trans. R. Soc. Lond. 356 (1998) 3123–3184.
[48] P.A. Madsen, O.R. Sørensen, A new form of the Boussinesq equations with improved linear dispersion characteristics. Part 2: a slowing varying bathymetry, Coast. Eng. 18 (1992) 183–204.
[49] J.H. Mathews, K.K. Fink, Numerical Methods Using Matlab, Prentice-Hall Inc., New Jersey, USA, 2004.
[50] D.E. Mitsotakis, B. Ilan, D. Dutykh, On the Galerkin/finite-element method for the Serre equations, J. Sci. Comput. 61 (2014) 166–215.
[51] J. Murillo, P. Garcia-Navarro, J. Burguete, Time step restrictions for well-balanced shallow water solutions in non-zero velocity steady states, Int. J. Numer. Methods Fluids 60 (2009) 1351.
[52] J. Murillo, P. Garcia-Navarro, J. Burguete, P. Brufau, The influence of source terms on stability, accuracy and conservation in two-dimensional shallow flow simulation using triangular finite volumes, Int. J. Numer. Methods Fluids 54 (2007) 543.
[53] I.K. Nikolos, A.I. Delis, An unstructured node-centered finite volume scheme for shallow water flows with wet/dry fronts over complex topography, Comput. Methods Appl. Mech. Eng. 198 (2009) 3723–3750.
[54] O. Nwogu, An alternative form of the Boussinesq equations for nearshore wave propagation, J. Waterw. Port Coast. Ocean Eng. 119 (1994) 618–638.
[55] O. Nwogu, Numerical prediction of breaking waves and currents with a Boussinesq model, in: Proceedings 25th International Conference on Coastal Engineering, 1996.
[56] J. Orszaghova, A.G.L. Borthwick, P.H. Taylor, From the paddle to the beach – a Boussinesq shallow water numerical wave tank based on Madsen, and Sørensen's equations, J. Comput. Phys. 231 (2012) 328–344.
[57] M. Parsani, D.I. Ketcheson, W. Deconinck, Optimized explicit Runge–Kutta schemes for the spectral difference method applied to wave propagation problems, SIAM J. Sci. Comput. (2) (2013) A957–A986.
[58] M. Ricchiuto, An explicit residual based approach for shallow water flows, J. Comput. Phys. 280 (2015) 306–344.
[59] M. Ricchiuto, A. Bollermann, Stabilized residual distribution for shallow water simulations, J. Comput. Phys. 228 (2009) 1071–1115.
[60] M. Ricchiuto, A.G. Filippini, Upwind residual discretization of enhanced Boussinesq equations for wave propagation over complex bathymetries, J. Comput. Phys. 271 (2014) 306–341.
[61] P.L. Roe, Approximate Riemann solvers, parameter vectors, and difference schemes, J. Comput. Phys. 43 (1981) 357–372.
[62] V. Roeber, K.F. Cheung, M.H. Kobayashi, Shock-capturing Boussinesq-type model for nearshore wave processes, Coast. Eng. 57 (2010) 407–423.
[63] V. Roeber, K.F. Cheung, Boussinesq-type model for energetic breaking waves in fringing reef environment, Coast. Eng. 70 (2012) 1–20.
[64] Y. Saad, Iterative Methods for Sparse Linear Systems, PWS, 1996.
[65] H.A. Schäffer, P.A. Madsen, R. Deigaard, A Boussinesq model for waves breaking in shallow water, Coast. Eng. 20 (1993) 185–202.
[66] F.J. Sebra-Santos, D.P. Renouard, A.M. Temperville, Numerical and experimental study of the transformation of a solitary wave over a self or isolated obstacle, J. Fluid Mech. 185 (1987) 523–545.
[67] F. Shi, J.T. Kirby, J.C. Harris, J.D. Geiman, S.T. Grilli, A high-order adaptive time-stepping TVD solver for Boussinesq modeling of breaking waves and coastal inundation, Ocean Model. 43–44 (2012) 36–51.
[68] O.R. Sørensen, H.A. Schäffer, P.A. Madsen, Surf zone dynamics simulated by a Boussinesq type model: Part III. Wave-induced horizontal nearshore circulations, Coast. Eng. 33 (1998) 155–176.
[69] G. Strang, On the construction and comparison of difference schemes, SIAM J. Numer. Anal. 5 (1968) 506–517.
[70] C.E. Synolakis, The run up of solitary waves, J. Fluid Mech. 185 (1987) 532–545.
[71] C.E. Synolakis, E.N. Bernard, V.V. Titov, U. Kanoglu, F.I. Gonzalez, Standards, criteria, and procedures for NOAA evaluation of tsunami numerical models, NOAA Tech. Memo. OAR PMEL-135, NOAA/Pacific Marine Environmental Laboratory, Seattle, WA, 2007.
[72] M. Tissier, P. Bonneton, F. Marche, F. Chazel, D. Lannes, A new approach to handle wave breaking in fully non-linear Boussinesq models, Coast. Eng. 67 (2012) 54–66.
[73] M. Tonelli, M. Petti, Hybrid finite-volume finite-difference scheme for 2DH improved Boussinesq equations, Coast. Eng. 56 (2009) 609–620.
[74] M. Tonelli, M. Petti, Finite volume scheme for the solution of 2D extended Boussinesq equations in the surf zone, Ocean Eng. 37 (2010) 567–582.
[75] M. Tonelli, M. Petti, Simulation of wave breaking over complex bathymetries by a Boussinesq model, J. Hydraul. Res. 49 (2011) 473–486.
[76] M. Tonelli, M. Petti, Shock-capturing Boussinesq model for irregular wave propagation, Coast. Eng. 61 (2012) 8–19.
[77] M. Walkey, M. Berzins, A finite element method for the two-dimensional extended Boussinesq equations, Int. J. Numer. Methods Fluids 39 (2002) 865.
[78] N.P. Waterson, H. Deconinck, Design principles for bounded higher-order convection schemes? A unified approach, J. Comput. Phys. 224 (1) (2007) 182–207.
[79] G. Wei, J.T. Kirby, A time-dependent numerical code for extended Boussinesq equations, J. Waterw. Port Coast. Ocean Eng. 120 (1995) 251–261.
[80] G. Wei, J.T. Kirby, S.T. Grilli, R. Subramanya, A fully nonlinear Boussinesq model for surface waves. Part 1. Highly nonlinear unsteady waves, J. Fluid Mech. 294 (1995) 71.
[81] G. Wei, J.T. Kirby, A. Sinha, Generation of waves in Boussinesq models using a source function approach, Coast. Eng. 36 (1999) 271.
[82] Y. Xing, X. Zhang, C.-W. Shu, Positivity-preserving high order well-balanced discontinuous Galerkin methods for the shallow water equations, Adv. Water Resour. 33 (12) (2010) 1476–1493.
[83] X. Zhang, Y. Xia, C.-W. Shu, Maximum-principle-satisfying and positivity-preserving high order discontinuous Galerkin schemes for conservation laws on triangular meshes, J. Sci. Comput. 50 (2012) 29–62.